

Delayed resonator for complete vibration suppression of primary structures with nonlinear stiffness

Yifan Liu, Li Cheng*

Department of Mechanical Engineering, The Hong Kong Polytechnic University, Kowloon, Hong Kong, China

ARTICLE INFO

Keywords:

Active vibration control
Delayed resonator
Nonlinear stiffness
Delay-coupled nonlinear dynamics
Stability

ABSTRACT

Delayed resonator (DR) is an active vibration absorber and is known for its complete vibration suppression capability by manipulating the feedback loop delay. This work aims to extend the DR concept from the widely considered linear applications to suppress vibrations on primary structures with nonlinear stiffness, based on the motivation that absolute linearity does not exist and nonlinearity is inherent in many structures to be protected. The nonlinearity stems from the commonly seen nonlinear symmetrical restoring forces. Threefold objectives are pursued: (1). To generalize the tuning mechanism of the DR and the dynamical analysis of the system to the nonlinear case. (2). To evaluate the effect of such nonlinearity on system dynamics and vibration suppression. (3). To enhance control performance by properly constructing nonlinearity and, accordingly, to establish the design criteria. Without loss of generality, a widely considered three-spring-two-link model is borrowed as an example for constructing the stiffness nonlinearity. Then, an exclusive resultant-based calculation procedure is introduced to efficiently handle the delay-coupled nonlinear dynamics. Besides, the feedback tuning for complete vibration suppression and the related stability issues are tackled, showing that the nonlinearity can significantly extend the operable frequency band while posing no extra demands on the control law. Based on the parameters of an actual experimental setup, numerous comparisons between linear and nonlinear cases are performed to demonstrate how the DR settles a nonlinear primary structure and, furthermore, how such nonlinearity can affect control performance and how it can be utilized to enhance vibration suppression.

1. Introduction

The delayed resonator (DR) was invented by Olgac and Holm-Hansen [1] in 1994 for vibration absorption, a typical example that time delay can counter-intuitively play a positive role in engineering applications. The exclusive feature of the DR is that it actively configures the inherent loop delay so that we can simultaneously tune the equivalent stiffness and damping of the system by monitoring a single absorber state for feedback actuation, thus enhancing the control robustness. Compared to the prototype of the dynamical vibration absorber (DVA) by Frahm [2], which was undamped and only operated near its natural frequency, the DR can track variable vibration frequency by tuning the feedback gain and delay in real-time. Moreover, the properly tuned DR yields complete vibration suppression compared with the classic DVA by Den Hartog and Ormondroyd [3], who additionally injected a damper into the DVA for a broader suppression region but compromised the efficacy of vibration suppression.

The control logic of the DR can be implemented by cooperating with various feedback states, e.g., position [1], acceleration [4],

and angular [5]. Note that the delayed control logic endowed single-mass absorbers with the capacity to completely suppress multiple-frequency vibrations [6], an exclusive strength of this logic over the classic PD control that similarly altered system's equivalent stiffness and damping, see also [7] for comparisons between such two control logics. Researchers are now demanding more from the DR than just vibration suppression. For instance, Nia and Sipahi [8] designed a delay-independent stable controller to cope with delay perturbations. Alsalem and Younis [9] used delayed control to settle a MEMS resonator undergoing strong fractal dynamics. Eris et al. [10] proposed a control logic consisting of both delayed and nondelayed terms to expedite response speed. To suppress measurement noises, Pilbauer et al. [11], Kučera et al. [12], and Liu et al. [13] adopted a distributed-delayed logic so that the feedback actuation depended on the sum of all the absorber states within a designated past time interval. Later, Vyhřídál et al. [14] compared the DR behaviors when the feedback actuation cooperated with different absorber states and evaluated the effect of sensory deficiencies in detecting the vibration frequency,

* Corresponding author.

E-mail address: li.cheng@polyu.edu.hk (L. Cheng).

see also [15,16] for handling such issues. Cai et al. [17,18] further established the connection between the tuning mechanism associated with different absorber states using the fractional-order operator and enhanced the DR performance by designing the fractional order, see also [19] for an enhanced DR design using a mechanical lever component. The DR concept is also generalized to have multiple degrees of freedoms (MDOF) to achieve the so-called non-collected vibration absorption [20–23], i.e., the DR position can differ from the vibration suppression point. One can also refer to [24–26] for the DR suppressing multiple-dimensional vibrations in robotic applications.

We notice that most DR studies to date so far have focused on the vibration control of primary structures with linear stiffness. However, absolute linearity does not exist in practice, and strong nonlinearity is in fact inherent in many structures to be protected. One well-investigated and commonly seen structural nonlinearity is the high-static-low-dynamic-stiffness (HSLDS) or its special case called quasi-zero-stiffness (QZS). The associated primary structures are usually of deformation or stress and exhibit a high natural frequency when settled and a low one if excited, exemplified by the loaded cantilever beam in [27], or see more examples from the textbooks [28,29], where such nonlinearity are mathematically depicted by the Duffing equation. Furthermore, such nonlinearity has been widely found to benefit vibration isolation [30–39], and the additional introduction of delayed feedback actuation further enhances the isolation performance. For instance, Sun et al. [40–45], Cheng et al. [46,47], Yan et al. [48], Huang et al. [49], Liu et al. [50], and Cai et al. [51] reported various delayed nonlinear vibration isolators. However, vibration isolators are usually SDOF structures, and dynamics become more complex when considering an absorption system due to the increased degree of freedom stemming from an additional mechanical absorber. Indeed, Zhao and Xu [52] enhanced a nonlinear absorption system using delayed control. Mao and Ding [53] optimized delayed control for broadband vibration suppression. Nonetheless, these studies focus more on analyzing parametric effects on vibration suppression, whereas how to specifically tune the control parameters as in linear DR cases to suppress vibrations at a designated frequency has not been enough discussion. For this, Wang et al. [54] designed an absorption system with a nonlinear primary structure to achieve such vibration suppression following the DR logic and experimentally verified the effectiveness. However, the feedback actuator in [54] is installed between the absorber and the fixed base rather than the absorber and the primary structure, which yields a simplified design problem but would pose restrictions in engineering practice since it may be hard to find a fixed plane for actuator installation.

Based on a 2DOF vibration absorption model in which the DR actuator is coupled with a nonlinear primary structure, we aim to establish more general theories to extend the DR concept to completely suppress harmonic vibrations on nonlinear primary structures. One difficulty is that the analysis in the Laplace domain widely used in existing DR studies is no longer available due to nonlinearity, and it is further complicated by the coupling between the DR actuation and the nonlinear primary structure and the transcendentality introduced by the delay. This issue is tackled by combining our recently proposed resultant-based procedure [55] with the harmonic balance method [56,57]. In addition, the nonlinearity of the primary structure here is not only taken as an inherent constant of natural structures but also an artificial parameter signifying structural modification of linear or weakly nonlinear structures to enhance vibration control. To this end, the considered nonlinear primary structure follows a classic three-spring-two-link model [40,58] to show how one can practically construct beneficial nonlinearity, with Duffing equation [28,29] deployed for stiffness truncation, leading to our threefold contributions: (i). We introduce calculation tools to study the complex delay-coupled nonlinear dynamics. (ii). We establish design rules for enhanced complete vibration suppression from perspectives of feedback actuation tuning, equilibrium stability, and control performance. (iii). We show

how the nonlinearity of the primary structure affects system behaviors and how, if possible, engineers can design such nonlinearity to achieve enhanced performance.

This paper is structured as follows. Section 2 establishes the mathematical model and the problems to be handled. Section 3 calculates frequency responses based on the resultant concept. The design rules of the DR are addressed in Section 4. Section 5 copes with equilibrium stability. Section 6 evaluates the parametric effect on vibration suppression. Illustrative numerical cases are studied in Section 7. Section 8 draws conclusions. Italic symbols without a bar superscript ‘ $\bar{\square}$ ’ are dimensionless quantities.

2. Problem formation

The classic DR configuration is depicted in Fig. 1(a), where a linear primary structure with stiffness \bar{k}_p is excited by a harmonic force \bar{f}_e , and a delayed feedback actuation \bar{u} is injected into a vibration absorber to achieve complete vibration suppression $|\bar{x}_p| \rightarrow 0$. A general form of the primary structures with nonlinear stiffness and with the resulting restoring forces symmetric about the equilibrium $\bar{x}_p = 0$ is shown in Fig. 1(b), in which the nonlinear restoring forces follow an odd function

$$\bar{F}_N(\bar{x}_p) = \bar{k}_p \bar{x}_p + \bar{k}_n \bar{x}_p^3 + \bar{k}_{n,5} \bar{x}_p^5 + \bar{k}_{n,7} \bar{x}_p^7 + \dots, \quad (1)$$

where \bar{k}_n , $\bar{k}_{n,5}$, and $\bar{k}_{n,7}$ are stiffness related to nonlinear motions. Since the aim is complete vibration suppression to achieve $|\bar{x}_p| \rightarrow 0$ by properly tuning \bar{u} , we only keep the first two terms so that $\bar{F}_N(\bar{x}_p)$ reduces to

$$\bar{F}_N(\bar{x}_p) = \bar{k}_p \bar{x}_p + \bar{k}_n \bar{x}_p^3, \quad (2)$$

which is the well-known Duffing-type restoring forces [29] and governs the nonlinear stiffness characteristics of a large range of structures [28, 29], such as the deflected beam, the beam with plane stress, and the pendulum. Particularly, we need to suppress rotary vibrations if the primary structure is a pendulum, and the associated DR structure can be referred to [5].

Values of \bar{k}_p and \bar{k}_n are usually related to each other in a practical structure, so we consider a typical three-spring-two-link model following [40,58] to practically construct the nonlinearity in the form of (2), leading to Fig. 1(c). Compared to the linear primary structure in Fig. 1(a), the nonlinear one is additionally connected to two horizontal springs \bar{k}_h via two links of length \bar{l} . The vertical spring \bar{k}_p suspends the primary structure, and the horizontal two \bar{k}_h are pre-compressed by \bar{h} . Note that we step further from [54], where the actuator \bar{u} is coupled between the absorber and the base. Meanwhile, the shown nonlinear construction is an implementable structural modification of linear primary structures to enhance vibration suppression using nonlinearity, another focus of this work, see [59] for an alternative using magnetic springs. Besides, it signifies a potential application of the DR to enhance the nonlinear vibration isolation from the primary structure to the base or vice versa.

2.1. Governing equations

Dynamics of the 2-DOF coupled system in Fig. 1(c), consisting of a primary structure and an absorber, are governed by

$$\begin{cases} \bar{m}_a \ddot{\bar{x}}_a + \bar{c}_a (\dot{\bar{x}}_a - \dot{\bar{x}}_p) + \bar{k}_a (\bar{x}_a - \bar{x}_p) = \bar{u}, \\ \bar{m}_p \ddot{\bar{x}}_p + \bar{c}_p \dot{\bar{x}}_p + \bar{F}(\bar{x}_p) + \bar{c}_a (\dot{\bar{x}}_p - \dot{\bar{x}}_a) + \bar{k}_a (\bar{x}_p - \bar{x}_a) = \bar{f}_e - \bar{u}, \end{cases} \quad (3)$$

where $\bar{x}_{(\cdot)}$, $\bar{m}_{(\cdot)}$, $\bar{c}_{(\cdot)}$, and $\bar{k}_{(\cdot)}$ is the absolute displacement, mass, damping, and stiffness, respectively; the subscripts $(\cdot)_a$ and $(\cdot)_p$ denote the absorber and the primary structure, respectively; the dot notation means calculating derivatives with respect to the physical time, \bar{t} ;

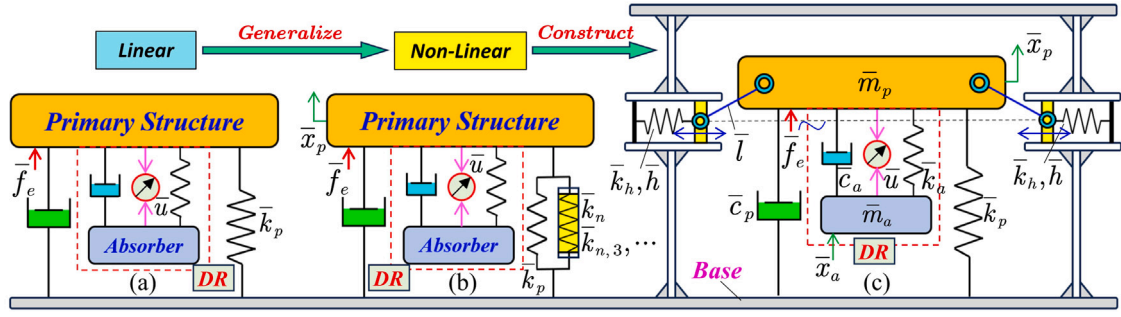


Fig. 1. (a). A classic DR configuration with a linear primary structure. (b). DR mounted on a primary structure with nonlinear symmetry stiffness. (c). A practical construction for the nonlinear primary structure in subplot (b).

$\bar{F}(\bar{x}_p)$ is the total nonlinear restoring force by three linear springs of the primary structure [58],

$$\bar{F}(\bar{x}_p) = \bar{k}_p \bar{x}_p - 2\bar{k}_h \left[\bar{h} - \left(\bar{l} - \sqrt{\bar{l}^2 - \bar{x}_p^2} \right) \right] \frac{\bar{x}_p}{\sqrt{\bar{l}^2 - \bar{x}_p^2}}, \quad (4)$$

which is an odd function of \bar{x}_p . Introducing the following scaled symbols

$$\begin{aligned} \bar{\omega}_p &= \sqrt{\bar{k}_p / \bar{m}_p}, \bar{\omega}_a = \sqrt{\bar{k}_a / \bar{m}_a}, \zeta_p = \frac{\bar{c}_p}{2\bar{m}_p \bar{\omega}_p}, \zeta_a = \frac{\bar{c}_a}{2\bar{m}_a \bar{\omega}_a}, \\ \mu &= \frac{\bar{m}_a}{\bar{m}_p}, \nu = \frac{\bar{\omega}_a}{\bar{\omega}_p}, k = \bar{k}_h / \bar{k}_p, \end{aligned} \quad (5)$$

$$\begin{aligned} h &= \bar{h} / \bar{l}, t = \bar{l} / \bar{\omega}_p, x_a = \bar{x}_a / \bar{l}, x_p = \bar{x}_p / \bar{l}, F = \bar{F} / (\bar{k}_p \bar{l}), \\ f_e &= \bar{f}_e / (\bar{k}_p \bar{l}), u = \bar{u} / (\bar{k}_p \bar{l}), \end{aligned}$$

into (3) leads to the dimensionless governing equations

$$\begin{cases} \mu [\ddot{x}_a + 2\zeta_a \nu (\dot{x}_a - \dot{x}_p) + \nu^2 (x_a - x_p)] = u, \\ \ddot{x}_p + 2\zeta_p \dot{x}_p + F(x_p) + 2\mu \zeta_a \nu (\dot{x}_p - \dot{x}_a) + \mu \nu^2 (x_p - x_a) = f_e - u, \end{cases} \quad (6)$$

in which the dimensionless restoring force F takes the form of

$$F(x_p) = x_p - 2k \left(h - 1 + \sqrt{1 - x_p^2} \right) \frac{x_p}{\sqrt{1 - x_p^2}}. \quad (7)$$

To support the primary structure at $x_p = 0$, negative stiffness should be avoided at this point, leading to

$$K(x_p = 0) = \partial F(x_p) / \partial x_p |_{x_p=0} = 1 - 2kh \geq 0. \quad (8)$$

Otherwise, the primary structure cannot be settled at $x_p = 0$ even if it is slightly perturbed [55]. Furthermore, it is claimed following [40,58] to be quasi-zero-stiffness (QZS) around $x_p = 0$ when $K(x_p = 0) = 0$, and the coupled system retreats to the classic linear setup in Fig. 1(a) when $k = 0$.

2.2. Duffing-type dynamics coupled with delayed feedback actuation

The feedback actuation follows the classic position-based control logic of the DR prototype [1] for comparisons,

$$\bar{u} = \bar{g} \bar{x}_a (\bar{l} - \bar{\tau}), \quad (9)$$

where \bar{g} is the gain and $\bar{\tau}$ is the actively introduced delay, two control parameters. Substituting (9) into (6) arrives at

$$\begin{cases} \mu [\ddot{x}_a + 2\zeta_a \nu (\dot{x}_a - \dot{x}_p) + \nu^2 (x_a - x_p)] = g x_a (t - \tau), \\ \ddot{x}_p + 2\zeta_p \dot{x}_p + F(x_p) + 2\mu \zeta_a \nu (\dot{x}_p - \dot{x}_a) + \mu \nu^2 (x_p - x_a) \\ = f_e - g x_a (t - \tau), \end{cases} \quad (10)$$

where the two dimensionless control parameters (g, τ) satisfy

$$g = \bar{g} / \bar{k}_p, \tau = \bar{\tau} \bar{\omega}_p. \quad (11)$$

Since the DR is tuned to completely settle the primary structure at $x_p = 0$, around which $F(x_p)$ can be rationalized by the third-order

Maclaurin series (i.e., the Taylor series expanded at $x_p = 0$) with a high enough accuracy [40,51,55,58],

$$F(x_p) \approx F_a(x_p) = \sum_{i=0}^3 \frac{f^{(i)}}{i!} x_p^i = n_0 + n_1 x_p + n_2 x_p^2 + n_3 x_p^3, \quad (12)$$

where $n_1 = 1 - 2hk = K(x_p = 0)$, $n_3 = k(1 - h)$, and $n_0 = n_2 = 0$ since $F(x_p)$ is an odd function. Note that the form of the rationalized (12) agrees with the Duffing force in (2). Plugging (12) into (10), the governing equations are reshaped as

$$\begin{cases} \dot{x}_a = x_{a,d}, \\ \dot{x}_a = \frac{g}{\mu} x_a (t - \tau) - 2\zeta_a \nu (x_{a,d} - x_{p,d}) - \nu^2 (x_a - x_p), \\ \dot{x}_p = x_{p,d}, \\ \dot{x}_p = f_e - g x_a (t - \tau) - 2\zeta_p x_{p,d} - \mu \nu^2 (x_p - x_a) \\ - 2\mu \zeta_a \nu (x_{p,d} - x_{a,d}) - F_a(x_p), \end{cases} \quad (13)$$

where $x_{a,d}$ and $x_{p,d}$ are the absolute velocity of the absorber and the primary structure, respectively. Letting $\dot{x}_a = \dot{x}_p = 0$ and $\ddot{x}_a = \ddot{x}_p = 0$, one can find from (13) that $(x_a, x_p) = (0, 0)$ is a pair of equilibria. We stress that maintaining the equilibria should be taken as a hard requirement for the design and tuning of the control logic to facilitate device installation in practice. The accuracy of dynamical prediction using the approximate Eq. (13) for the original system (10) is verified in Section 3.3.

Now, three parameters (k, g, τ) compared with a linear passive 2-DOF vibration absorption system are newly introduced. The problems of interest are threefold: (i). How does the nonlinearity reflected in $k > 0$ of the primary structure affect system dynamics? (ii). If possible, how to properly tune the control parameter pair (g, τ) when $k > 0$ to achieve complete vibration suppression as in linear cases? (iii). If possible, how can we design the nonlinearity k to enhance vibration suppression?

3. Harmonic dynamics analysis

We focus on the system dynamics when the primary structure is excited by a harmonic force in the dimensionless form of

$$f_e(\omega, t) = A_e \sin(\omega t) = \frac{\bar{A}_e}{\bar{k}_p \bar{l}} \sin\left(\frac{\bar{\omega}}{\bar{\omega}_p} \bar{l} \bar{\omega}_p\right), \quad (14)$$

where $\bar{A}_e > 0$ and $\bar{\omega} > 0$ is the practical amplitude and frequency of the force excitation \bar{f}_e , respectively, and A_e and ω are the associated dimensionless parameters as per (5). Note that the dynamical analysis is complicated by the coupling of the delayed feedback actuation \bar{u} between the primary structure and the absorber. Besides, the widely used Laplace transform-based analysis in existing DR studies for linear applications is no longer operable once the nonlinearity $k > 0$ is introduced. To this end, the resultant-based procedure of our recent work [55] is generalized to benefit calculation.

3.1. Resultant-based frequency response analysis

Different from linear cases where the input and output frequencies are identical, the dynamics of the considered nonlinear model excited by (14) satisfy a Fourier series expression according to the harmonic balance method [56,57],

$$x_\psi(t) = \sum_{i=0}^{\infty} (A_{\psi,i} \cos(i\omega t) + B_{\psi,i} \sin(i\omega t)), \psi = [a, p], \quad (15)$$

where $\psi = a$ and $\psi = p$ denote the absorber and primary structure, respectively. Since most steady-state energy is concentrated on the first harmonic, i.e., $i = 1$ in Eq. (15), which is even more so when we aim to keep the steady-state motion amplitude of the nonlinear primary structure within a low enough level given that the nonlinear forces are small around $x_p = 0$, the dominant responses are also harmonic at the fundamental frequency ω but with a different amplitude and phase so that

$$\begin{cases} x_a(\omega, t) = R_a(t) \sin(\omega t + \phi_a) \\ \quad = A_a(t) \sin(\omega t) + B_a(t) \cos(\omega t), \\ x_p(\omega, t) = R_p(t) \sin(\omega t + \phi_p) \\ \quad = A_p(t) \sin(\omega t) + B_p(t) \cos(\omega t), \end{cases} \quad (16)$$

where ϕ_a and ϕ_p are phase differences, A_a, B_a, A_p , and B_p are slowly-varying real coefficients, and $R_a = \sqrt{A_a^2 + B_a^2}$ and $R_p = \sqrt{A_p^2 + B_p^2}$ are the associated motion amplitudes. Substituting Eqs. (14) and (16) into (10), the coefficients of the $\sin(\omega t)$ and $\cos(\omega t)$ terms should vanish, resulting in four equations that can be represented in a matrix form of

$$\mathbf{P}(\omega) \boldsymbol{\Theta} = \mathbf{G}_{4 \times 1}(\omega, \boldsymbol{\Theta}^T), \quad (17)$$

where $\boldsymbol{\Theta} = [A_a, B_a, A_p, B_p]^T$, \mathbf{G} is matrix in $(\omega, \boldsymbol{\Theta}^T)$, and

$$\mathbf{P}(\omega) = 2 \begin{bmatrix} -\mu v \zeta_a & \mu \omega & \mu v \zeta_a & 0 \\ -\mu \omega & -\mu v \zeta_a & 0 & \mu v \zeta_a \\ \mu v \zeta_a & 0 & -\mu v \zeta_a - \zeta_p & \omega \\ 0 & -\mu v \zeta_a & -\omega & -\mu v \zeta_a - \zeta_p \end{bmatrix}. \quad (18)$$

Since $\dot{\boldsymbol{\Theta}} \equiv \mathbf{0}$ holds in the steady state $t \rightarrow \infty$, we consider $\mathbf{G}(\omega, \boldsymbol{\Theta}^T) = \mathbf{0}$, yielding

$$\begin{cases} G_1(\omega, \boldsymbol{\Theta}^T) = \mu((A_a - A_p)v^2 - 2\omega \zeta_a(B_a - B_p)v - A_a\omega^2) \\ \quad - g(A_a C + B_a S) = 0, \\ G_2(\omega, \boldsymbol{\Theta}^T) = \mu((B_a - B_p)v^2 + 2\omega \zeta_a(A_a - A_p)v - B_a\omega^2) \\ \quad - g(B_a C - A_a S) = 0, \\ G_3(\omega, \boldsymbol{\Theta}^T) = 3n_3 A_p^3 + (3n_3 B_p^2 + \vartheta) A_p \\ \quad - 8(\zeta_a v(B_p - B_a)\mu + \zeta_p B_p)\omega - 4(A_a(\mu v^2 - gC) - gB_a S + A_e) = 0, \\ G_4(\omega, \boldsymbol{\Theta}^T) = 3n_3 B_p^3 + (3n_3 A_p^2 + \vartheta) B_p \\ \quad - 8(\zeta_a v(A_a - A_p)\mu - \zeta_p A_p)\omega - 4(g(SA_a - CB_a) + \mu v^2 B_a) = 0, \end{cases} \quad (19)$$

where $S = \sin(\omega\tau)$, $C = \cos(\omega\tau)$, and $\vartheta = 4(\mu v^2 - \omega^2 + n_1)$. The common solution composition $(\omega, \boldsymbol{\Theta}^T)$ then dictates the frequency responses. However, directly solving the coupled nonlinear Eq. (19) without initial guesses is cumbersome. Given a frequency ω , we take $G_1(\omega, \boldsymbol{\Theta}^T) = 0$ and $G_2(\omega, \boldsymbol{\Theta}^T) = 0$ as two linear equations in (A_p, B_p) , which can be solved as

$$\begin{cases} A_p(\omega, A_a, B_a) = \frac{A_a \mu v^3 + (\mu A_a (4\zeta_a^2 - 1)\omega^2 - g(A_a C + B_a S))v - 2(\mu B_a \omega^2 + g(CB_a - SA_a))\zeta_a \omega}{\mu v(4\omega^2 \zeta_a^2 + v^2)}, \\ B_p(\omega, A_a, B_a) = \frac{B_a \mu v^3 + (\mu B_a (4\zeta_a^2 - 1)\omega^2 - g(CB_a - SA_a))v - 2(\mu A_a \omega^2 + g(CA_a + SB_a))\zeta_a \omega}{\mu v(4\omega^2 \zeta_a^2 + v^2)}. \end{cases} \quad (20)$$

Substituting the solution pair (A_p, B_p) given in (20) into $G_3(\omega, \boldsymbol{\Theta}^T) = 0$ and $G_4(\omega, \boldsymbol{\Theta}^T) = 0$ leads to

$$\begin{cases} G_3(\omega, A_a, B_a) = C_f(\omega) \sum_{i=0}^3 \alpha_i(\omega, B_a) A_a^i = 0, \\ G_4(\omega, A_a, B_a) = C_f(\omega) \sum_{i=0}^3 \beta_i(\omega, B_a) A_a^i = 0, \end{cases} \quad (21)$$

where $C_f(\omega) = \omega^2 \zeta_a^2 + v^2/4$ is a common factor, α_i and β_i are coefficients in (ω, B_a) . We use the notation $\deg[p, x]$ to denote the highest degree of the variable x in a polynomial p , yielding $\deg[\alpha_i, B_a] = \deg[\beta_i, B_a] = 3$ and $\deg[\alpha_i, \omega] = \deg[\beta_i, \omega] = 7$. The problem now reduces to seeking the solution pair (A_a, B_a) of Eq. (21) for a given ω . However, closed-form solutions are still inaccessible due to the coupling between A_a and B_a . Alternatively, we adopt the Sylvester resultant concept [60] to avoid numerical solutions. Since $C_f(\omega) \neq 0$, the Sylvester matrix between the two equations in (21) is

$$\mathbf{S}(\omega, B_a) = \text{res}_{A_a} \left(\frac{G_3}{C_f}, \frac{G_4}{C_f} \right) = \begin{bmatrix} \alpha_3 & \alpha_2 & \alpha_1 & \alpha_0 & 0 & 0 \\ 0 & \alpha_3 & \alpha_2 & \alpha_1 & \alpha_0 & 0 \\ 0 & 0 & \alpha_3 & \alpha_2 & \alpha_1 & \alpha_0 \\ \beta_3 & \beta_2 & \beta_1 & \beta_0 & 0 & 0 \\ 0 & \beta_3 & \beta_2 & \beta_1 & \beta_0 & 0 \\ 0 & 0 & \beta_3 & \beta_2 & \beta_1 & \beta_0 \end{bmatrix} \quad (22)$$

leading to the Sylvester resultant equation

$$R(\omega, B_a) = |\mathbf{S}(\omega, B_a)| = \sum_{i=0}^3 \gamma_i(\omega) B_a^i = 0, \quad (23)$$

which is a polynomial equation in (ω, B_a) , and we have $\deg[\gamma_i, \omega] = 40$. The Sylvester resultant provides a necessary condition for two polynomial equations to have common solutions [61]. That is, all the solution pairs (ω, B_a) of Eq. (21) for any A_a value constitute a subset of those of Eq. (23). Accordingly, such a resultant-based procedure for the solution composition $(\omega, A_a, B_a, A_p, B_p)$ of Eq. (19) by sweeping the frequency ω is summarized in Fig. 2, where the two steps ① and ② handle univariate polynomial equations that can be easily solved without needing initial guesses [62], and the checking step corresponds to the necessary condition, see more details in [55] where a non-delayed SDOF system is considered.

3.2. Stability of frequency response solutions

Nonlinearity can lead to multiple solutions (A_a, B_a, A_p, B_p) for a given frequency ω , while a practical system can only settle at the stable ones. The stability test following [63] is briefly reviewed for coherence. We rewrite Eq. (17) as

$$\dot{\boldsymbol{\Theta}} = \mathbf{H}_{4 \times 1}(\omega, \boldsymbol{\Theta}^T), \quad (24)$$

where $\mathbf{H}(\omega, \boldsymbol{\Theta}^T) = \mathbf{P}^{-1}(\omega) \mathbf{G}(\omega, \boldsymbol{\Theta}^T)$. The stable solutions labeled as $\boldsymbol{\Theta}_s$ for any ω means $\boldsymbol{\Theta}^T \rightarrow \boldsymbol{\Theta}_s$ as $t \rightarrow \infty$, and thus all the eigenvalues of the Jacobian matrix

$$\mathbf{J}_{4 \times 4}(\omega, \boldsymbol{\Theta}^T) = \frac{\partial \mathbf{H}(\omega, \boldsymbol{\Theta}^T)}{\partial \boldsymbol{\Theta}}, \quad (25)$$

must have negative real parts at $(\omega, \boldsymbol{\Theta}_s)$. Hence, the stable solution compositions $(\omega, \boldsymbol{\Theta}_s)$ of Eq. (19) are defined as

$$(\omega, \boldsymbol{\Theta}_s) = \left\{ (\omega, \boldsymbol{\Theta}^T) \mid \left\{ \begin{array}{l} \mathbf{G}(\omega, \boldsymbol{\Theta}^T) = \mathbf{0}, \\ \text{Re}(\text{veig}(\mathbf{J}(\omega, \boldsymbol{\Theta}^T))) < 0. \end{array} \right. \right\}, \quad (26)$$

where $\text{Re}(\cdot)$ and $\text{eig}(\cdot)$ represent the operations of getting the real part and calculating eigenvalues, respectively.

3.3. Verification

The basic parameters of the considered coupled system shown in Fig. 1(c) are borrowed from a linear experimental vibration absorption system constructed in [11,12] to benefit comparisons, with

$$\begin{aligned} \bar{m}_a &= 0.223 \text{ kg}, \bar{c}_a = 1.273 \text{ kg/s}, \bar{k}_a = 350 \text{ N/m}, \\ \bar{m}_p &= 1.520 \text{ kg}, \bar{c}_p = 10.11 \text{ kg/s}, \bar{k}_p = 1960 \text{ N/m}. \end{aligned} \quad (27)$$

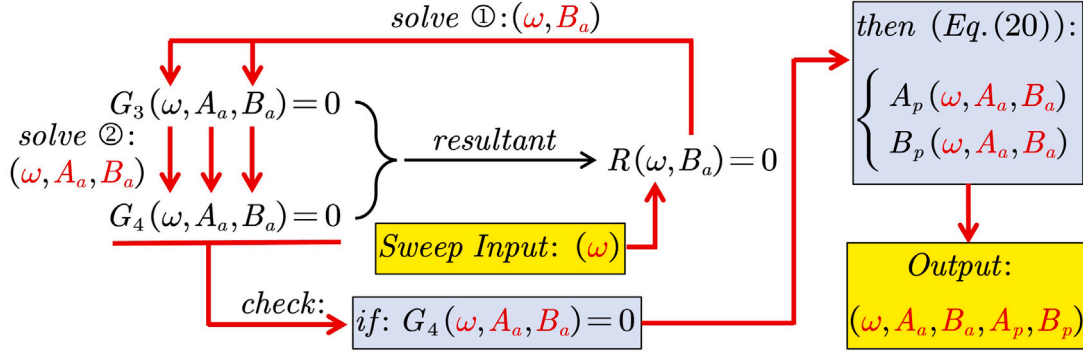


Fig. 2. Resultant-based univariate solving procedures for the common solution composition $(\omega, A_a, B_a, A_p, B_p)$.

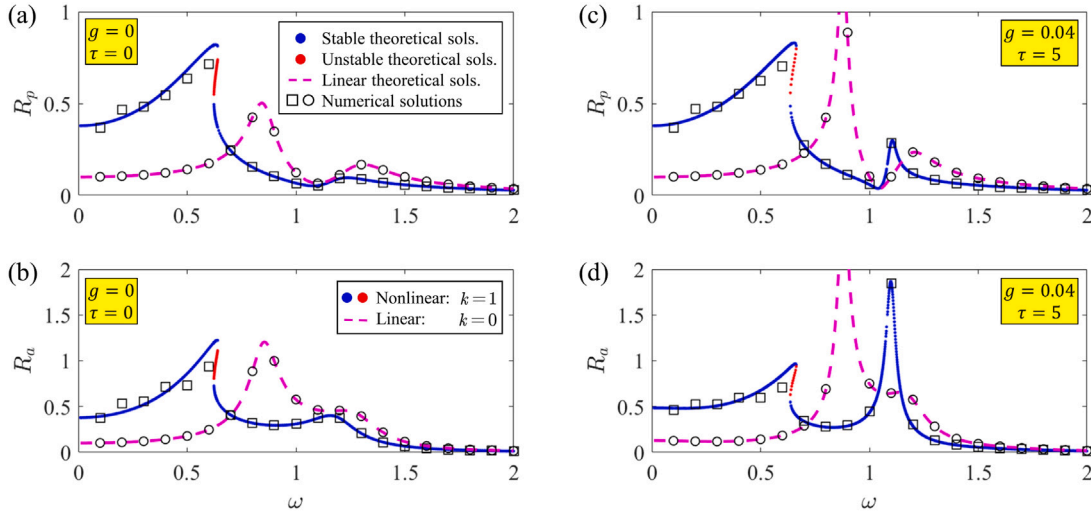


Fig. 3. Comparisons between the theoretical and numerical frequency responses of the coupled system (28) for $A_e = 0.1$. (a-b). Passive case with $(g, \tau) = (0, 0)$. (c-d). Active case with $(g, \tau) = (0.04, 5)$.

Besides, the length of the two additional links and the precompression of the two additional horizontal springs \bar{k}_h are arbitrarily fixed as $\bar{l} = 0.1$ m and $\bar{h} = 0.04$ m, respectively, leading to

$$\begin{aligned} \mu &= 0.147, \bar{\omega}_p = 35.91, \bar{\omega}_a = 39.62, \nu = 1.1, \\ \zeta_p &= 0.093, \zeta_a = 0.072, h = 0.4. \end{aligned} \quad (28)$$

Hence, the three tunable parameters (k, g, τ) correspond to $(\bar{k}_h, \bar{g}, \bar{\tau})$. Selecting the excitation amplitude as $A_e = 0.1$, the frequency responses $(\omega, A_a, B_a, A_p, B_p)$ or equivalently (ω, R_a, R_p) for four (k, g, τ) compositions are verified in Fig. 3.

The theoretical solutions in Fig. 3 are obtained by the resultant-based solving procedure specified in Fig. 2, and the stability is checked by Eq. (26). The numerical solutions are constituted by the steady states of the frequency responses calculated by MATLAB SIMULINK, with the exact restoring force $F(x_p)$ in (7) deployed for verification. Clearly, theoretical solutions well predict the numerical ones, and a smaller motion amplitude R_p yields higher prediction accuracy, which favorably matches the desired goal of complete vibration suppression $R_p = 0$ in steady states. Although the accuracy slightly decreases in the low-frequency band where the primary structure exhibits large amplitudes due to the limited truncations of the rationalization series (12) and the harmonic balance method (15), the trends of system dynamics there are still well-predicted. Furthermore, the linear frequency responses denoted by magenta dashed curves in Fig. 3 are obtained by setting $k = 0$, and they concur with the results based on Laplace transform. Comparing the results in linear $(k = 0)$ and nonlinear $(k > 0)$ cases, one can conclude that the nonlinearity can raise low-frequency vibrations

while suppressing high-frequency ones. On the other hand, comparisons between Fig. 3(a) and (c) indicate that the delayed control can deepen the anti-resonance for potential complete vibration suppression of a nonlinear primary structure. More specific design rules of (k, g, τ) for this are considered next.

4. Parameter tuning for complete vibration suppression

In this part, we first tune the control parameter pair (g, τ) , aiming to completely suppress the dominant vibrations, i.e., the vibrations at the fundamental frequency ω , and such completeness is explained. Since dominance is numerically demonstrated in Section 7, we omit the term ‘dominant’ for simplicity. Besides, the mechanism of such vibration suppression is investigated.

4.1. Tuned control parameter pair

The aim is to properly tune (g, τ) so that $x_p = 0$ or equivalently $R_p = 0$ as per (16). From Eq. (20), we have

$$\begin{aligned} R_p^2(\omega, A_a, B_a) &= A_p^2 + B_p^2 \\ &= \frac{(A_a^2 + B_a^2) \left((v^2 - \omega^2)^2 + 4\zeta_a^2 \omega^2 v^2 \right) \mu^2 + g^2 + 2g\mu (2S\omega v \zeta_a + C(\omega^2 - v^2))}{(4\omega^2 \zeta_a^2 + v^2) \mu^2 v^2}. \end{aligned} \quad (29)$$

Since $R_a^2 = A_a^2 + B_a^2 \neq 0$ when achieving $x_p = 0$ for the absorber to neutralize the excitation force f_e , the condition $R_p = 0$ evolves from

Eq. (29) to

$$F(\omega, g, \tau) = g^2 + 2\mu\kappa_1(\omega, \tau)g + \mu^2\kappa_2(\omega) = 0, \quad (30)$$

where $\kappa_1(\omega, \tau) = 2\omega v\zeta_a \sin(\omega\tau) + (\omega^2 - v^2)\cos(\omega\tau)$ and $\kappa_2(\omega) = (v^2 - \omega^2)^2 + 4\zeta_a^2\omega^2v^2$. Since $g^2 + \mu^2\kappa_2(\omega) > 0$, the sign of $\kappa_1(\omega, \tau)$ must be opposite to that of the gain g . Note that $F(g) = 0$ is a parabolic equation in g , and the discriminant denoted by Δ of $F(g)$ satisfies

$$\Delta = 4\mu^2(\kappa_1^2(\omega, \tau) - \kappa_2(\omega)) \leq 0 \quad (31)$$

given the forms of $\kappa_1(\omega, \tau)$ and $\kappa_2(\omega)$. Consequently, Eq. (30) has a double root for g at most, so we construct

$$\kappa_1(\omega, \tau) = \begin{cases} -\sqrt{\kappa_2(\omega)}, g > 0, \\ \sqrt{\kappa_2(\omega)}, g < 0, \end{cases} \quad (32)$$

leading to the solution pair of Eq. (30) as

$$\begin{cases} g_t(\omega) = \pm\mu\sqrt{(v^2 - \omega^2)^2 + 4\zeta_a^2\omega^2v^2}, \\ \tau_{t,r}(\omega) = \frac{1}{\omega} \left(a \tan\left(\frac{-2\zeta_a\omega v}{v^2 - \omega^2}\right) + 2(r-1)\pi + \frac{|s_g| - s_g}{2}\pi \right), \end{cases} \quad (33)$$

where the subscript $(\cdot)_t$ means ‘tuned’, $s_g = \text{sign}(g_t(\omega)) = \pm 1$, and $r = 1, 2, \dots$ resulting from the periodicity of the two trigonometric terms, i.e., $\sin(\omega\tau) = \sin(\omega\tau \pm 2r\pi)$ and $\cos(\omega\tau) = \cos(\omega\tau \pm 2r\pi)$, is called branch number [14]. From the forms of $(g_t, \tau_{t,k})$, the nonlinearity $k > 0$ poses no effect on the tuning mechanism, agreeing with the approximation (15) that the nonlinear primary structure vibrates at the fundamental frequency ω and the linear property of the DR. Considering also that the harmonic balance method (15), regardless of orders, seeks steady-state solutions and since the nonlinear forces reduce as $|x_p| \rightarrow 0$, the vibration suppression by a operably tuned DR can be complete, as will be demonstrated in Section 7.

4.2. Tuned DR behaviors for complete vibration suppression

Assuming that complete vibration suppression $x_p = 0$ is achieved, the four governing equations in (19) reduce to

$$\begin{cases} G'_1(\omega, A_a, B_a) \\ = ((v^2 - \omega^2)\mu - g \cos(\omega\tau))A_a - (2\zeta_a\mu v\omega + g \sin(\omega\tau))B_a = 0, \\ G'_2(\omega, A_a, B_a) \\ = (2\zeta_a\mu v\omega + g \sin(\omega\tau))A_a + ((v^2 - \omega^2)\mu - g \cos(\omega\tau))B_a = 0, \\ G'_3(\omega, A_a, B_a) \\ = (g \cos(\omega\tau) - \mu v^2)A_a + (2\zeta_a\mu v\omega + g \sin(\omega\tau))B_a - A_e = 0, \\ G'_4(\omega, A_a, B_a) \\ = (2\zeta_a\mu v\omega + g \sin(\omega\tau))A_a - (g \cos(\omega\tau) - \mu v^2)B_a = 0, \end{cases} \quad (34)$$

where the superscript $(\cdot)'$ denotes the reduced case $x_p = 0$ to discriminate (34) from (19). Note that the common solution $(A_a, B_a) = (0, 0)$ of the three equations $\{G'_1 = 0, G'_2 = 0, G'_4 = 0\}$ holds only if $A_e = 0$ acting like the DR is mounted on a virtual ground. When $A_e \neq 0$, we construct

$$\begin{cases} G'_{1,3}(\omega, A_a) = G'_1 - G'_3 = -\mu A_a\omega^2 - A_e = 0, \\ G'_{2,4}(\omega, B_a) = G'_2 + G'_4 = -\mu B_a\omega^2 = 0, \end{cases} \quad (35)$$

which reflects two obvious conditions for the complete vibration suppression at ω

$$\begin{cases} \text{sign}(A_a) = -\text{sign}(A_e), \\ B_a = 0, \end{cases} \quad (36)$$

indicating that the phase of the DR motion x_a differs from that of the excitation f_e by π in light of the form of (16). That is, the damping force by \bar{c}_a is neutralized by the delayed feedback actuation \bar{u}' so that

the phase difference is half a cycle. Furthermore, the motion amplitude of the DR in this case according to (35) is explicitly governed by

$$R'_a(\omega) = |A_a(\omega)| = \frac{A_e}{\mu\omega^2} = \frac{\bar{m}_p\bar{A}_e\omega_p^2}{\bar{m}_a\bar{k}_p\bar{l}\bar{\omega}^2} = \frac{\bar{A}_e}{\bar{l}\bar{m}_a\bar{\omega}^2}, \quad (37)$$

which is independent of the primary structure agreeing with the linear case [4]. With Eqs. (16), (36), and (37), the force exerted on the primary structure from the resonant absorber via the damper \bar{c}_a and spring \bar{k}_a is

$$\begin{aligned} \bar{f}'_{a \rightarrow p}(\bar{\omega}, \bar{t}) &= \bar{k}_a\bar{x}'_a + \bar{c}_a\dot{\bar{x}}'_a \\ &= \bar{k}_aR'_a\bar{l}\sin(\bar{\omega}\bar{t}) + \bar{c}_aR'_a\bar{l}\bar{\omega}\cos(\bar{\omega}\bar{t}). \end{aligned} \quad (38)$$

To neutralize the force excitation \bar{f}'_e on the primary structure for complete vibration suppression by additionally applying the tuned feedback actuation \bar{u}' , we must have

$$\bar{f}'_{a \rightarrow p} - \bar{u}' - \bar{f}'_e = 0. \quad (39)$$

Substituting Eqs. (14) and (38) into (39) gives

$$\left(\frac{\bar{k}_a\bar{A}_e}{\bar{m}_a\bar{\omega}^2}\sin(\bar{\omega}\bar{t}) - \bar{u}'_1\right) + \left(\frac{\bar{c}_a\bar{A}_e}{\bar{m}_a\bar{\omega}}\cos(\bar{\omega}\bar{t}) - \bar{u}'_2\right) = \bar{A}_e\sin(\bar{\omega}\bar{t}). \quad (40)$$

The feedback actuation \bar{u}' is divided into two parts \bar{u}'_1 and \bar{u}'_2 in (40), in which \bar{u}'_2 neutralizes the damping force as per (36) and \bar{u}'_1 complements the difference between the excitation \bar{f}'_e and the force exerted on the primary structure through the spring \bar{k}_a by the absorber. Besides, we have $\bar{u}'_1 = 0$ when the natural frequency of the absorber equals the excitation frequency, i.e., $\bar{\omega}_a = \bar{\omega}$, and thus, in this case, the feedback actuation \bar{u}' is equivalent to an additional negative damper valued by $-\bar{c}_a$. Note also that such equivalence only holds at the tuning frequency. The relationship (40) reveals an important core of the DR, i.e., the DR can simultaneously alter system’s damping and stiffness via a single feedback state, e.g., the displacement x_a considered in (9), thus saving an observer and yielding stronger control robustness compared with the PD control [7].

5. Equilibrium stability and operable ranges of stiffness k and excitation frequency ω

The DR tuned with any control parameters (g, τ) should ensure a stable equilibrium $x_p = 0$. Such stability is called equilibrium stability to discriminate it from the stability of the frequency response solutions addressed in Section 3.2, where the pair (g, τ) is fixed. The equilibrium stability is analyzed using linearization theory performed at $x_p = 0$, around which the nonlinear primary structure vibrates. To achieve complete vibration suppression $|x_p| \rightarrow 0$, by a tuned DR, the operable range of the stiffness k denoting the nonlinearity and the operable range of the excitation frequency ω are both investigated.

5.1. Characteristic equation and operable stiffness range

To evaluate equilibrium stability, we consider the characteristic Jacobian matrix of (13),

$$\mathbf{J}_{CS}(x_p, \lambda, g, \tau, k) = \begin{bmatrix} 0 & 1 & 0 & 0 \\ \frac{g}{\mu}e^{-\lambda\tau} - v^2 & -2\zeta_a v & v^2 & 2\zeta_a v \\ 0 & 0 & 0 & 1 \\ -ge^{-\lambda\tau} + \mu v^2 & 2\mu\zeta_a v & -\mu v^2 - n_1(k) - 3n_3(k)x_p^2 & -2\mu\zeta_a v - 2\zeta_p \end{bmatrix}, \quad (41)$$

where λ is the characteristic variable. The characteristic equation of the coupled system at the equilibrium $x_p = 0$ is then

$$\begin{aligned} CE(\lambda, g, \tau, k) &= \left| \lambda \mathbf{I}_{4 \times 4} - \mathbf{J}(x_p = 0) \right| \\ &= (\mu(\lambda^2 + 2\zeta_a v \lambda + v^2) - ge^{-\tau\lambda})(\lambda^2 + 2\zeta_p \lambda + n_1(k)) \\ &\quad + \mu^2 \lambda^2 v (2\zeta_a \lambda + v) = 0. \end{aligned} \quad (42)$$

Note that k appears in the linear stiffness term $n_1(k) = 1 - 2hk$ defined in (12) to affect equilibrium stability. Furthermore, Eq. (42) has a stationary root $\lambda = 0$ when the primary structure is QZS (i.e., $n_1 = 0$). In linear cases, if $\lambda = 0$ is the rightmost root, then the coupled system has infinitely many equilibria. In the passive nonlinear case, the cubic stiffness term n_3 and the higher-order ones omitted in (12) produce nonlinear restoring forces since the excited primary structure yields $|x_p| \gg 0$, so an excited QZS primary structure still vibrates around $x_p = 0$. However, most excitation force f_e (external disturbance) is neutralized if an operable DR tuned by (33) is deployed, as mentioned in (39). Thus, a QZS primary structure requires a long time to converge from $|x_p| \rightarrow 0_+$ to $x_p = 0$ since linear restoring forces signified by $n_1 x_p$ are small and nonlinear ones related to higher-order terms of x_p are even smaller being close to zero. Consequently, we according to (8) prefer

$$k \in \left[0, \frac{1}{2h}\right) \quad (43)$$

to prevent the primary structure from being QZS for the complete vibration suppression at $x_p = 0$, which signifies an operable stiffness range if we are allowed to design the nonlinearity k . Numerical demonstrations for this are prepared in Section 7.2.

5.2. Stability map

To address stability issues, excluding the stationary root $\lambda = 0$ and separating variables, we can write Eq. (42) into

$$ge^{-\tau\lambda} = \mu(\lambda^2 + 2\zeta_a v\lambda + v^2) + \frac{\mu^2 \lambda^2 v(2\zeta_a \lambda + v)}{(\lambda^2 + 2\zeta_p \lambda + n_1(k))}. \quad (44)$$

The spectrum of Eq. (42) or Eq. (44) for any parameter composition (k, g, τ) must lie on the left half of the complex plane for stability. According to the D-subdivision method [64], stability loses and regains at the critical moment when the characteristic Eq. (42) or (44) exhibits a pair of imaginary roots, say $\lambda = \pm j\omega_c$, where $\omega_c \in \mathbb{R}^+$ is the frequency of the resulting Hopf bifurcation. Hence, all control parameter pairs (g, τ) satisfying $CE(\lambda = j\omega_c, g, \tau, k) = 0$ constitute stability boundaries. Substituting $\lambda = j\omega_c$ into (44) and separating the real and imaginary parts lead to

$$ge^{-j\tau\omega_c} = \sigma(\omega_c, k) + j\varpi(\omega_c, k), \quad (45)$$

where $\sigma(\omega_c, k)$ and $\varpi(\omega_c, k)$ are real functions and are self-evident from (44). Consequently, the stability boundaries satisfy

$$\begin{cases} g_c(\omega_c, k) = \pm\sqrt{\sigma^2(\omega_c, k) + \varpi^2(\omega_c, k)}, \\ \tau_{c,q}(\omega_c, k) = \frac{1}{\omega_c} \left(a \tan\left(\frac{-\varpi(\omega_c, k)}{\sigma(\omega_c, k)}\right) + 2(q-1)\pi + \frac{|s_{gc}|^{-s_{gc}}}{2}\pi \right), \end{cases} \quad (46)$$

where $s_{gc} = \text{sign}(g_c)$, and $q = 1, 2, \dots$ stems from the periodicity of the complex exponent $e^{-j\tau\omega_c}$ similar to the branch number r in (33). Given the forms of $(g_r, \tau_{r,q})$ and $(g_c, \tau_{c,q})$, one can conclude that the nonlinearity $k > 0$ affects equilibrium stability although it does not affect the tuning law of the DR. For the coupled system (28), the tuned pairs $(g_r, \tau_{r,q})$ and the stability boundaries $(g_c, \tau_{c,q})$ in the linear ($k = 0$) and the nonlinear ($k = 1$) cases with sweeping $(\omega, \omega_c) \in \mathbb{R}^{2+}$ are superposed in Fig. 4.

Let us first focus on the stability boundaries $(g_c, \tau_{c,q})$ denoted by the solid curves. Considering that a passive system with $g = 0$ is stable as per (8) and the infinitely small feedback actuation $|g| \rightarrow 0^+$ is unable to alter system dynamics, the shown colored regions must be stable since stability alternation or Hopf bifurcation can only occur at the stability boundaries. Once we cross stability boundaries, the corresponding imaginary root $\lambda = \pm j\omega_c$ can either shift to the right half of the complex plane leading to instability or limited cycles, or return to the left [64]. The shifting directions can be checked by the root tendency [65],

$$R_T = \left(\text{Re}\left(\frac{\partial\lambda}{\partial s}\Big|_{\lambda=j\omega_c}\right)\right), \quad (47)$$

where $s \in [g, \tau]$ represents the crossing variable, and $R_T = +1$ and $R_T = -1$ signify that the imaginary root pair $\pm j\omega_c$ shifts rightward and leftward, respectively. To this end, the exhaustive stable regions, as colored in Fig. 4, can be determined by counting the number of unstable characteristic roots in each parametric region divided by stability boundaries. Clearly, any operable control parameter pair (g, τ) must lie within the stable regions.

Remark 1. When the harmonic external excitation f_e is introduced, the stable regions in the nonlinear case $k > 0$ obtained as per Fig. 4 should be taken as the necessary conditions for determining the operable pairs of (g, τ) since analysis is based on equilibrium stability. To focus on the effect of k on vibration suppression, we assume that orbits of the excited primary structure can be captured by the basin of attraction of a stable equilibrium, indicating that the complex counterexamples (not shown in our extensive numerical examinations based on the manipulatable SIMULINK models provided in the Appendix) are excluded in this work, i.e., f_e is taken as a small periodic disturbance. This agrees with the truncations at the third-order series performed in (2) and (12). Furthermore, in this sense, if the DR is tuned for complete vibration suppression, the stable location of the tuned pair $(g_r, \tau_{r,q})$ in Fig. 4 provides high enough accuracy for its operability since $x_p = 0$ is the unique equilibrium and the condition $|x_p| \rightarrow 0$ leads to very small nonlinear forces in steady states. ■

5.3. Stability map

With Remark 1, we next investigate the operability of a tuned DR, and the associated tuned pairs $(g_r, \tau_{r,q})$ are superposed as the dashed curves in Fig. 4. Operable tuned pairs must render a stable equilibrium, exemplified by the three segments P_0P_1 , P_2P_3 , and P_4P_5 for $k = 0$ and the three $P'_0P'_1$, $P'_2P'_3$, and $P'_4P'_5$ for $k = 1$. Particularly, the two points P_0 and P'_0 are not shown due to coordinate limitations. Note from Eq. (33) that the tuned pair $(g_r, \tau_{r,q})$ is a function of the excitation frequency ω once given a k , and thus equilibrium stability limits the operable frequency ranges for the desired complete vibration suppression. Moreover, the operable frequencies for each operable segment are governed by the frequencies corresponding to the two ends of this segment since the tuned pair $(g_r, \tau_{r,q})$ is continuous to ω .

We take the intersection point P_1 as an example. It corresponds to an identical pair of control parameters (g, τ) but two different values of ω and ω_c . Consequently, the intersection condition yields

$$\begin{cases} g_r(\omega, k) - g_c(\omega, k) = 0, \\ \tau_{r,q}(\omega_c, k, r) - \tau_{c,q}(\omega_c, k, q) = 0, \end{cases} \quad (48)$$

two equations in $(\omega, \omega_c) \in \mathbb{R}^{2+}$ once given a k and a pair of branch numbers (r, q) and thus can be numerically solved. Since an unduly large delay is unfavorable to robustness [14] and since the width of the operable segments reduces as branch number r increases, we only consider the smallest r that yields positive tuned delays, i.e., $r = 1$ for $g < 0$ and $r = 2$ for $g > 0$. By sweeping $k \in [0, 1.25]$, the operable frequency ranges for the coupled system (28) are depicted in Fig. 5(a).

The six intersection points $P_1, P_2, P_3, P'_1, P'_2$, and P'_3 in Fig. 4 are marked in Fig. 5(a) to show the connection between such two stability maps. From Fig. 5(a), smaller tuned delays yield broader operable frequency ranges, although the branch number r does not affect the tuned gain amplitude $|g_r|$. In both cases $g < 0$ and $g > 0$, increasing k from the linear case $k = 0$ extends operable low-frequency ranges. As k further increases, the low-frequency bound ω_{low} , as marked in the figure, nearly stops varying once it exceeds a threshold value (i.e., $k = 0.44$ for $g > 0$ and $k = 0.79$ for $g < 0$). This property agrees with the forms of the stability boundaries $(g_c, \tau_{c,q})$ and the tuned pairs $(g_r, \tau_{r,q})$, given that n_1 reduces as k increases, thus posing fewer effects on $(g_c, \tau_{c,q})$ as ω_c decreases, see (44) and (46). Moreover, the tuned pair $(g_r, \tau_{r,q})$ is independent of k , and therefore the intersection between

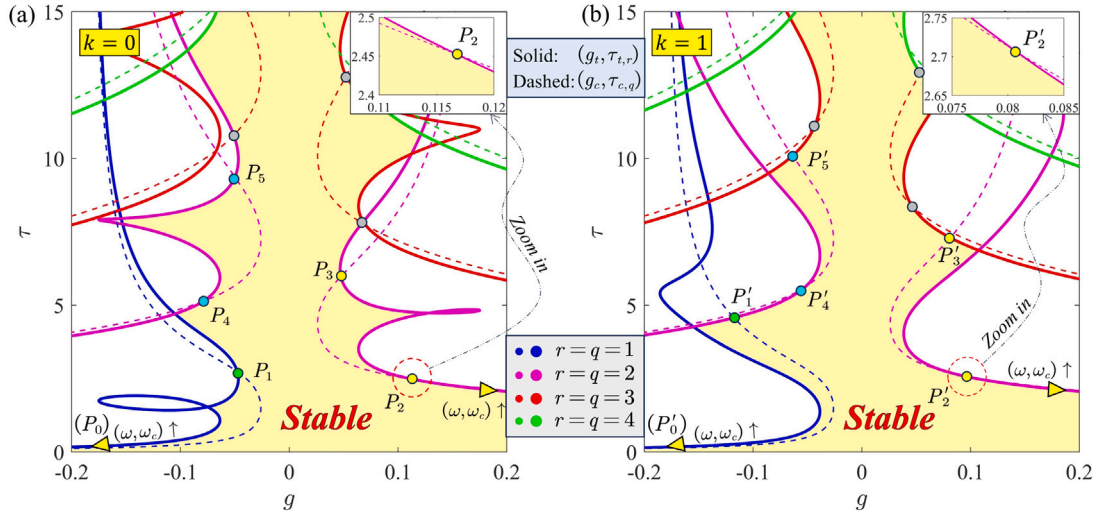


Fig. 4. Equilibrium stability of the coupled system (28). (a) Linear case with $k = 0$. (b) Nonlinear case with $k = 1$. Colored regions are stable. Solid and dashed curves represent the stability boundaries $(g_c, \tau_{c,q})$ and the tuned pairs $(g_i, \tau_{i,r})$, respectively. (For interpretation of the references to color in this figure legend, the reader is referred to the web version of this article.)

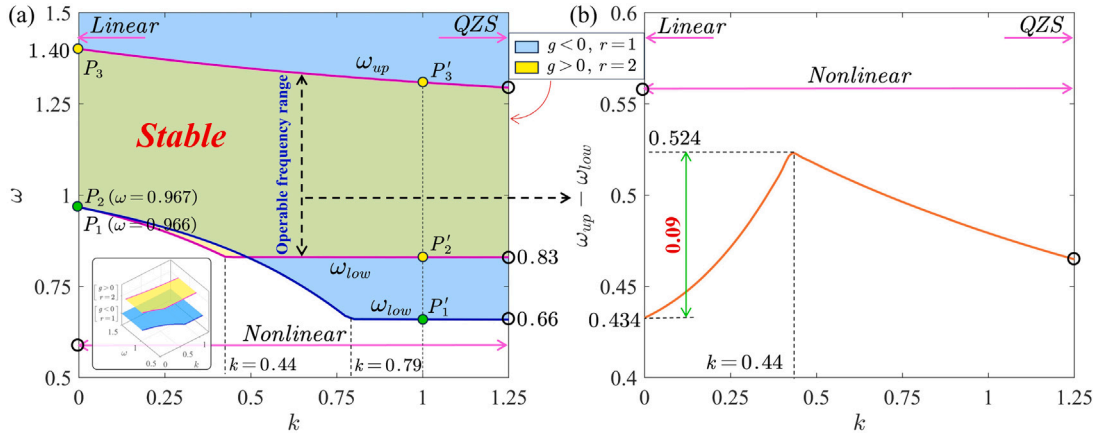


Fig. 5. (a). Operable frequency bands versus k for $(g < 0, r = 1)$ and $(g > 0, r = 2)$. (b). Operable frequency bandwidth associated with (a). The cases $k = 0$ and $k = 1.25$ correspond to the linear and QZS primary structures, respectively.

$(g_c, \tau_{c,q})$ and $(g_i, \tau_{i,r})$ tends to be fixed as k increases. On the other hand, the fact that the broadest operable frequency range appears at a limited value of k is beneficial since a larger k means harder horizontal stiffness \bar{k}_h , which can be difficult to practically implement if the stiffness \bar{k}_p of the primary structure is already large, let alone that we need to avoid the QZS case as per (43), i.e., the shown case $k = 1/(2h) = 1.25$.

More specifically, the operable low-frequency bound for $(g < 0, r = 1)$ is extended by $(0.966 - 0.66)/0.966 \approx 31\%$ by having $k = 0.79$. The width of the operable frequency range for $(g > 0, r = 2)$ is shown in Fig. 5(b), indicating that it can be extended by 21% when $k = 0.44$. The significant effect of k on the operable bandwidth indicates that simply ignoring the inherent nonlinearity of a primary structure can lead to conservative results. However, for stability concerns, it is safe to tune a DR to handle low-frequency vibrations by assuming a linear primary structure since ω_{low} decreases as k increases around $k = 0$. More attention should be paid when ω raises since the operable upper bound ω_{up} also decreases as k increases. More specifically, the operable low-frequency bound for $(g < 0, r = 1)$ is extended by $(0.966 - 0.66)/0.966 \approx 31\%$ by having $k = 0.79$. The width of the operable frequency range for $(g > 0, r = 2)$ is shown in Fig. 5(b), indicating that it can be extended by 21% when $k = 0.44$. The significant effect of k on the operable bandwidth indicates that simply ignoring the inherent nonlinearity of a primary structure can lead to conservative results.

However, for stability concerns, it is safe to tune a DR to handle low-frequency vibrations by assuming a linear primary structure since ω_{low} decreases as k increases around $k = 0$. More attention should be paid when ω raises since the operable upper bound ω_{up} also decreases as k increases.

Remark 2. A crucial and well-known difference between linear and nonlinear dynamics is that frequency responses in nonlinear cases can exhibit a multiple-state frequency band [29], see Fig. 3. Clearly, operable frequencies should lie outside such bands for robust complete vibration suppression. However, most vibrations of the nonlinear primary structure are suppressed by an operable tuned DR, and therefore the two horizontal springs \bar{k}_h produce negligible nonlinear forces in the vertical direction in steady states. From this perspective, the multiple-state frequency band does not affect the operable frequencies in Fig. 5(a). ■

6. Parametric effects

Having established the tuning mechanism and obtained the operable frequency interval, we next consider how an operable tuned DR suppresses vibrations and how the nonlinearity of the primary structure affects system performance. The topics are twofold: (i). The frequency

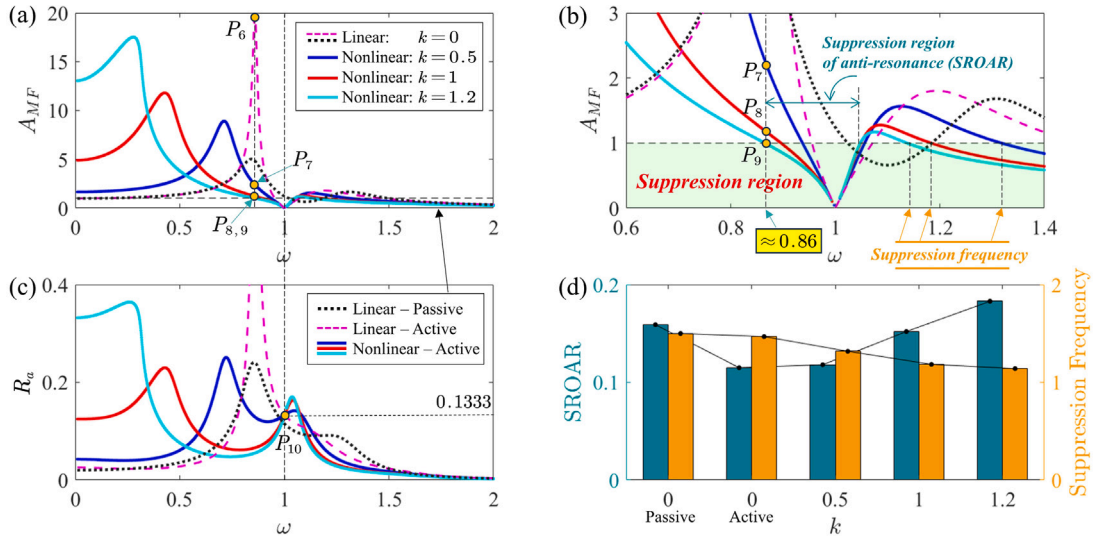


Fig. 6. Comparisons related to different k values when the DR is tuned at $\omega = 1$ with ($g < 0, r = 1$). (a). The A_{MF} versus k . (b). The zoomed plot of (a). (c). Frequency responses of the absorber versus k . (d). The indices of (b), where SROAR refers to suppression region of anti-resonance.

responses of the coupled system, and (ii). The settling time of the transient process.

6.1. Effect of nonlinearity $k > 0$ on frequency responses

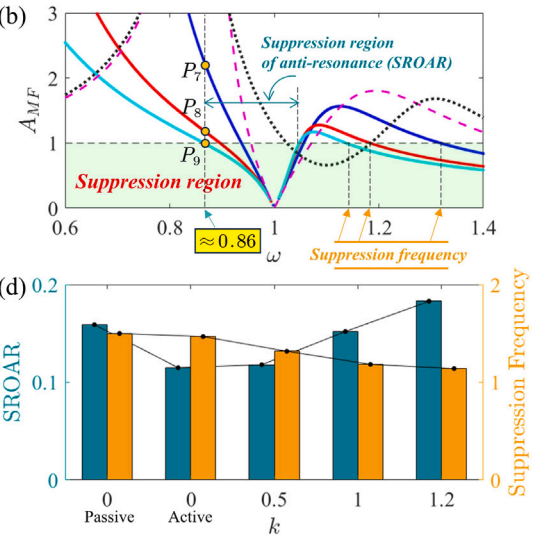
Following the linear case [66], we convert the dimensional frequency response amplitude $|\bar{x}_p(\omega)|$ of the primary structure to the dimensionless amplitude amplification factor (AMF) for generality,

$$A_{MF}(\omega) = \frac{|\bar{x}_p(\omega)|}{\bar{A}_e/\bar{k}_p} = \frac{R_p(\omega)\bar{l}}{A_e\bar{l}} = \frac{R_p(\omega)}{A_e}, \quad (49)$$

which depicts the vibration suppression performance of the absorber compared with the associated SDOF primary structure that is only supported by a linear spring \bar{k}_p . Clearly, smaller values of $A_{MF}(\omega)$ yield better suppression performance, effective vibration suppression ensues with $A_{MF}(\omega) < 1$, and the complete suppression by a tuned DR leads to $A_{MF}(\omega) = 0$.

For the coupled system (28), we select $A_e = 0.02$, thus yielding $\bar{A}_e = A_e\bar{k}_p\bar{l} = 3.92$ N to streamline with [11,12]. The AMF and the frequency responses R_a of the absorber when the DR is tuned at $\omega = 1$ are shown in Fig. 6, where the branch ($g < 0, r = 1$) corresponding to the smallest positive tuned delay is considered. The operability of the tuned pairs for different k values can be referred to the stability map in Fig. 5(a).

From Fig. 6(a), compared with the passive case $g = 0$, the tuned DR shifts the anti-resonance interval to the designated frequency $\omega = 1$ and suppresses the anti-resonance to zero, regardless of the nonlinearity k . Note that the resulting zero anti-resonance leads to higher resonance peaks shifting to lower frequencies as k increases, thus achieving the effect of a low-pass filter with an amplification mechanism. Consequently, when ω increases from the low-frequency band over the first resonance frequency, the A_{MF} value of a nonlinear primary structure is much smaller than that in the linear case $k = 0$, as featured in the magnitude condition $P_6 > P_7 > P_8 > P_9$ of Fig. 6(a), see also the zoomed plot in Fig. 6(b). This property helps suppress high-frequency noises commonly caused by mechanical equipment. Meanwhile, the low-pass effect means low-frequency excitations deserve much attention if the nonlinearity of the primary structure is non-negligible. Also, comparing the linear case $k = 0$ and the nonlinear one $k = 0.5$ concludes that, if possible, we can utilize the nonlinearity by properly designing k to suppress the resonance peak while keeping the raised A_{MF} in the low-frequency band within a limited value.



The frequency responses of the absorber are compared in Fig. 6(c), where all the response curves in the active cases (i.e., the tuned DR is activated) intersect at a fixed point P_{10} with $R_a(\omega = 1) = 0.1333$, concurring with (37) that is independent of k . Moreover, comparisons between Fig. 6(c) and Fig. 6(a) show that a higher motion amplitude of the primary structure does not necessarily correspond to a higher absorber amplitude, signifying the phase difference between such two components. The A_{MF} around $\omega = 1$ is zoomed in Fig. 6(b), from which one can find that the nonlinearity introduced by $k > 0$ favorably extends the suppression region where $A_{MF} < 1$ of both the anti-resonance interval and the high-frequency interval quantified by the suppression frequency defined in Fig. 6(b), see also the more detailed comparisons in Fig. 6(d). We stress that the extended suppression region of anti-resonance (SROAR) enhances control robustness, especially considering that the excitation f_e in practice can drift or be noisy, which leads to frequency mismatches. More specific comparisons are performed in Section 7.3.

6.2. Effect of nonlinearity $k > 0$ on transient behaviors

In this part, we aim to expedite the transient process to settle the excited primary structure as fast as possible, a topic widely considered in both linear [10,17] and nonlinear [40,42,43] cases. Provided that the periodic solutions can be captured by a stable equilibrium as per Remark 1 or vibrations are caused by impact, the key is to place the dominant (i.e., the rightmost) root labeled as λ_{dom} of the characteristic Eq. (42) leftmost since the settling time can be approximated by

$$\bar{t}_s = t_s\bar{\omega}_p \text{ [s]}, \quad (50)$$

where t_s is the dimensionless form of \bar{t}_s and satisfies

$$t_s = -\frac{4}{\text{Re}(\lambda_{dom})}, \text{Re}(\lambda_{dom}) < 0. \quad (51)$$

We are then interested in the effect of the nonlinearity $k > 0$ on \bar{t}_s . However, no analytical solutions to the characteristic Eq. (42) exist due to transcendentality. Alternatively, we adopt the QPmR algorithm [67], which approximates the complex spectrum of a quasi-polynomial equation within a given region at a designated accuracy.

Following Fig. 5, we consider the coupled system (28) with a DR tuned with $\omega = 1$. The variations of $\text{Re}(\lambda_{dom})$ and the settling time \bar{t}_s for ($g < 0, r = 1$) and ($g > 0, r = 2$) with respect to $k \in [0, 1.25]$ are shown in Fig. 7(a) and (b).

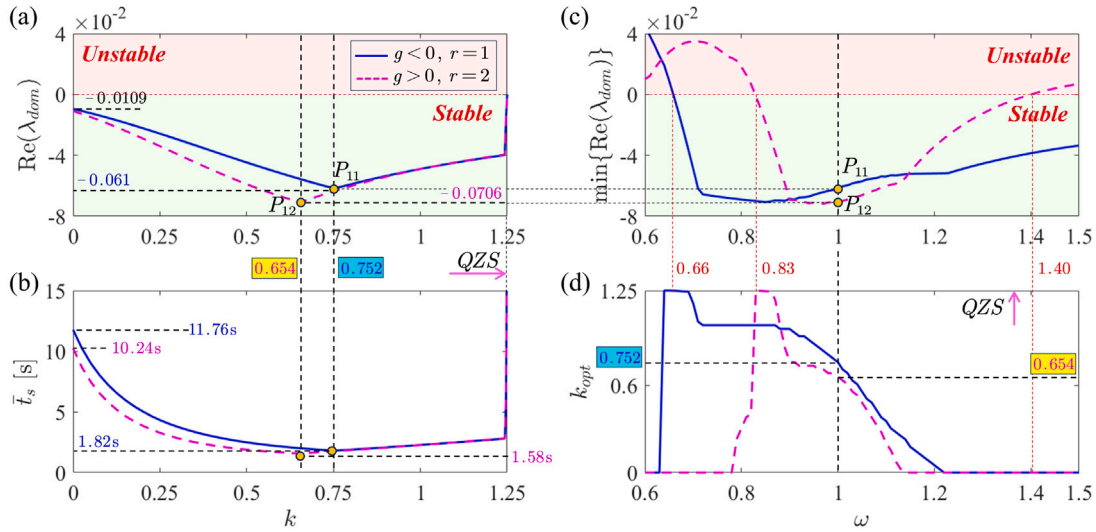


Fig. 7. Spectral analysis of Eq. (42) for the transient behaviors of the coupled system (28). (a). The real part of the dominant root λ_{dom} versus k for $\omega = 1$. (b). The theoretical settling time \bar{t}_s versus k for $\omega = 1$. (c). The generalized results of (a) by sweeping $\omega \in [0.6, 1.5]$. (d). The optimal values of k corresponding to the minima $\min\{\text{Re}(\lambda_{dom})\}$ in (c).

From Fig. 7(a), all the dominant roots λ_{dom} have negative real parts, agreeing with Fig. 5(a), where $\omega = 1$ always lies within the stable region regardless of $k \in [0, 1.25]$. Besides, we have $\text{Re}(\lambda_{dom}) \rightarrow 0$ as $k \rightarrow 1.25$, a direct result of the stationary root $\lambda = 0$ associated with the QZS characteristics, as mentioned in Section 5.1. Furthermore, in both cases $g < 0$ and $g > 0$, properly tuning the nonlinearity $k > 0$ can minimize $\text{Re}(\lambda_{dom})$. The resulting benefits are intuitively reflected in the settling time \bar{t}_s shown in Fig. 7(b), where $\bar{t}_s = 11.76$ s in the linear case $k = 0$ when $g < 0$ is significantly reduced by 84.52% to $\bar{t}_s = 1.82$ s by having $k = 0.752$. Similar results also hold when $g > 0$ so that $\bar{t}_s = 10.24$ s reduces to $\bar{t}_s = 1.58$ s as $k = 0$ increases to $k = 0.654$. Comparing Fig. 7(a) and Fig. 5(a), one can conclude that a broader operable frequency range due to a smaller tuned delay does not necessarily lead to a shorter settling time, a trade-off needed to be considered in practical DR applications. Note also that increasing the delay to reduce the settling time is a counter-intuitive observation, see also [68,69], and an unduly large delay is unfavorable to robustness [14].

Next, we generalize the results in Fig. 7(a) and (b) by sweeping ω , thus arriving at Fig. 7(c) and (d). The two points P_{11} and P_{12} marked in Fig. 7(c) concur with the namesake two in Fig. 7(a). Besides, the optimal k values corresponding to the minima $\min\{\text{Re}(\lambda_{dom})\}$ are shown in Fig. 7(d). Remarkably, the operable frequency ranges signified by the condition $\min\{\text{Re}(\lambda_{dom})\} < 0$ in Fig. 7(c) and the associated k values in Fig. 7(d) agree with the equilibrium stability map in Fig. 5(a).

As for the transient behaviors, Fig. 7(c) and (d) show that different frequencies ω correspond to different optima of k , and the benefits of the nonlinearity k on achieving a shorter settling time \bar{t}_s are reduced in the high-frequency band. This is guaranteed given that the motion amplitude of a force-excited primary structure reduces as ω increases, thus resulting in smaller nonlinear restoring forces. Beneficially, from Fig. 7(d), the optimal k values for a shorter \bar{t}_s increase as ω decreases, which agrees with the variation trend of the width of the operable low-frequency ranges previously shown in Fig. 5(a). Hence, properly designing the nonlinearity $k > 0$ can simultaneously achieve broadband complete low-frequency vibration suppression and expedite response speed. This provides useful guidance for the selection of k .

Remark 3 (Design Criteria of the Nonlinearity k). We have shown four design criteria for the nonlinearity k , or equivalently, the horizontal stiffness \bar{k}_h . (i). To avoid the QZS characteristics as per Eq. (43). (ii). To match the operable frequency ranges given in Fig. 5(a) with the

excitation frequency ω . (iii). To consider the low-pass effect, the suppression frequencies for broadband (incomplete) vibration reduction, and the control robustness (i.e., SROAR) for the complete vibration suppression following Fig. 6. (iv). To seek possibilities for expedited response speed as per Fig. 7. For the considered coupled system (28), a preferable range can be $k \in [0.4, 0.7]$, given that the vibration suppression performance can be enhanced without stimulating the low-pass effect too much. Besides, the revealed benefits of $k > 0$ show that mechanical advantages can significantly enhance DR performance, a topic of increasing research interest, see also [19-23]. ■

7. Numerical case study

Several numerical case studies for the coupled system (28) are performed to more intuitively demonstrate the established theories and the revealed effects of the nonlinearity of the primary structure on vibration suppression. The exact restoring force (4) is used to test the effectiveness of the given theories that are based on the series truncated in (12) and the harmonic balance method truncated in (15). In addition, the excitation amplitude is fixed as $A_e = 0.02$ (i.e., $\bar{A}_e = 3.92$ N) following [11,12]. The adopted manipulable simulation model based on MATLAB SIMULINK can be found in Appendix.

7.1. Extended operable frequency band of complete vibration suppression

Let us start with verifying the complete vibration suppression and the extended operable frequency band when $k > 0$ featured in Fig. 5. For the excitation at $\omega = 0.95$ or $\bar{\omega} = \omega\bar{\omega}_p = 5.43$ Hz, we tuned the DR with ($g > 0, r = 2$) without loss generality, yielding $(g, \tau_{1,2}) = (0.0512, 6.143)$ or equivalently, $(\bar{g}, \bar{\tau}_{1,2}) = (100.36$ N/m, 171.1 ms). Spectra of the characteristic Eq. (42) calculated by the QPMR algorithm [67] and dynamics of the coupled system in the linear case $k = 0$ and the nonlinear case $k = 1$ (i.e., $\bar{k}_h = 1980$ N/m) are compared in Fig. 8.

From Fig. 8(a), a part of characteristic roots in the linear case $k = 0$ lies on the right half of the complex plane, leading to instability and agreeing with the stability map in Fig. 5(a). The resulting unstable dynamics are reflected in the divergence of the blue curves in Fig. 8(c) and (d). Besides, the frequency spectrum of the responses \bar{x}_p of the primary structure by fast flouier transform (FFT) is depicted in Fig. 8(b), where the frequency component at $\bar{\omega} = 5.43$ Hz is suppressed as expected, although the coupled system is unstable. Interestingly, a new component appears at $\bar{\omega} = 4.82$ Hz, which agrees with Fig. 8(d),

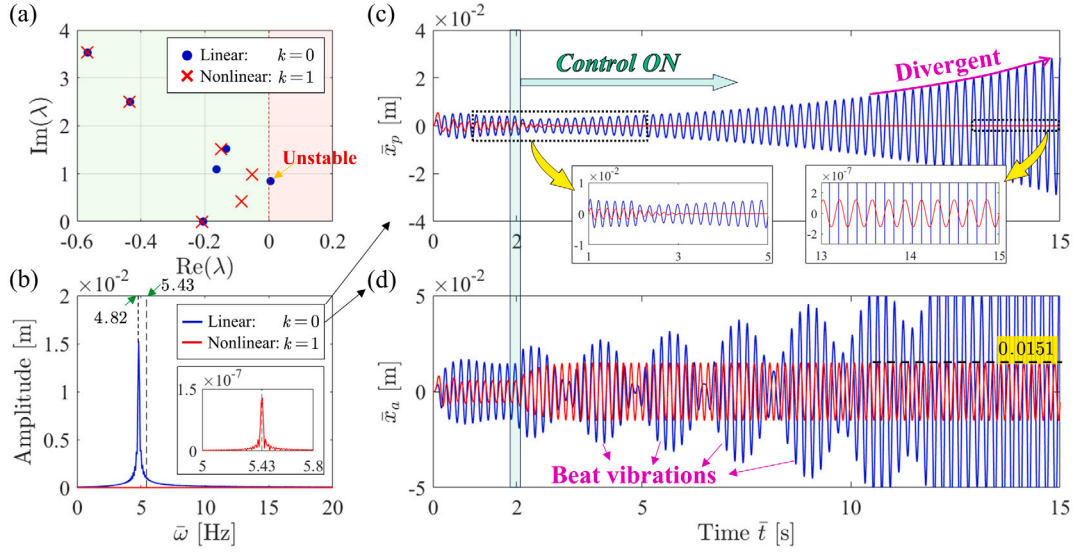


Fig. 8. Comparisons between the linear ($k = 0$) and nonlinear ($k = 1$) cases. (a). Spectra of the characteristic Eq. (42). (b). Frequency spectra of the primary structure using fast flourier transform. (c). Displacement responses of the primary structure. (d). Displacement responses of the absorber. The feedback actuation in (c) and (d) is activated at $\bar{t} = 2$ s.

where the absorber undergoes beat vibrations, an interference pattern between vibrations of slightly different frequencies.

As for the nonlinear case $k = 1$, the characteristic spectrum is stable as per Fig. 8(a), and the desired complete vibration suppression can be observed in Fig. 8(c). However, some small residual vibrations exist, as also detected by the FFT-based frequency spectrum in Fig. 8(b). Note that such residual vibrations are mainly caused by the limited simulation accuracy rather than the nonlinearity since the dominant frequency component concurs with the excitation frequency $\bar{\omega} = 5.43$ Hz, see Eq. (15). This inference agrees with the fact that the nonlinear restoring forces by the two springs \bar{k}_h are nearly zero as $|\bar{x}_p| \rightarrow 0$. It is also the reason why the vibration suppression of a nonlinear primary structure by a tuned DR can be claimed to be complete. Consequently, the nonlinearity $k > 0$ affects system dynamics and operable frequencies by altering transient behaviors instead of steady states, implying that one should not simply apply the results in linear DR studies based on the assumption $|x_p| \approx 0$. Besides, the motion amplitude $\bar{x}_a = 0.0151$ m of the absorber marked in Fig. 8(d) in the steady states concurs with (37). One should also notice that the amplitudes of the primary structure and the absorber in the linear case when no feedback actuation is introduced (i.e., $\bar{t} < 2$ s) are larger than those in the nonlinear case. Hence, the nonlinearity of the primary structure can benefit vibration suppression in both passive and active cases.

7.2. Deviated settling position of a QZS primary structure

Next, we consider the case where the nonlinear primary structure is QZS. Revisiting Section 5.1, the QZS properties render the characteristic Eq. (42) a stationary root $\lambda = 0$, and thus the settled primary structure can deviate from the equilibrium $\bar{x}_p = 0$. We still consider the DR tuned with ($g > 0, r = 2$) for $\omega = 0.95$, and spectra of Eq. (42) and performance of the coupled system when $k = [1.24, 1.25]$ or $\bar{k}_h = [2430.4 \text{ N/m}, 2450 \text{ N/m}]$ are compared in Fig. 9.

The stationary root $\lambda = 0$ in the QZS case $k = 1.25$ can be found in Fig. 9(a), and the associated vibration suppression performance is shown as the blue curves in Fig. 9(b), where the vibrating primary structure is settled once the feedback actuation is activated while the settling position deviates from $\bar{x}_p = 0$. The deviation mechanism can be interpreted as follows. Since the three springs ($\bar{k}_p, \bar{k}_h, \bar{k}_h$) and the damper \bar{c}_p of the primary structure provide null forces in the ideally settled case $\bar{x}_p \equiv 0$, the DR tuned as per (29) by letting $\bar{x}_p = 0$ yields

total forces via $(\bar{k}_a, \bar{c}_a, \bar{u})$, labeled as $\bar{f}_{a,total}$, that nearly neutralizes the excitation \bar{f}_e as $|\bar{x}_p| \rightarrow 0$, see also Eq. (39). Considering that the damping force by \bar{c}_p is small when \bar{x}_p does not vary much, the forces for the primary structure to finally converge to $\bar{x}_p = 0$ mainly depend on the spring composition $(\bar{k}_p, \bar{k}_h, \bar{k}_h)$, and thus a QZS primary structure can be hard to settle from the vicinity of $\bar{x}_p = 0$ to this point once a tuned DR is activated (note that QZS by definition means that stiffness around $\bar{x}_p = 0$ is nearly zero, see (8)). Such interpretation is verified in Fig. 9(c-e), where the convergence of the QZS primary structure after $\bar{t} \approx 5$ s only depends on restoring forces of springs, the small values of which lead to the deviated settling position in Fig. 9(b).

However, a QZS primary structure still converges to $\bar{x}_p = 0$ after a long time in the end since the stiffness $K(x_p)$ defined in (8) is always positive (although small) when $\bar{x}_p \neq 0$, and the stationary root $\lambda = 0$ only relates to the equilibrium $\bar{x}_p = 0$, see the derivation of Eq. (42). To this end, we select $k = 1.24$ to avoid a QZS primary structure, leading to no stationary root as in Fig. 9(a), and accordingly, the desired complete vibration suppression at $\bar{x}_p = 0$ is shown as the red curves in Fig. 9(b).

7.3. Suppression of the residual vibrations due to frequency mismatches

We now test the benefits of the extended suppression region of anti-resonance (SROAR) in Fig. 6 in suppressing the residual vibrations due to the mismatches between the detected excitation frequency and the actual one. Here, the DR is equipped with a frequency sensor whose resolution is larger than 0.1 Hz so that the DR cannot detect small variations in excitation frequency. Inspired by [15], we assume that the excitation frequency is theoretically known as $\omega = 1$ (i.e., $\bar{\omega} = 5.715$ Hz), while the actual one slightly varies from $\omega = 0.99$ to $\omega = 1.1$ following Fig. 10(a). We now tune the DR with ($g < 0, r = 1$) considering that a smaller delay benefits control robustness against frequency mismatches [14], thus leading to $(\bar{g}_t, \bar{\tau}_{t,1}) = (-77.39 \text{ N/m}, 69.89 \text{ ms})$. Responses \bar{x}_p of the primary structure for $k = [0, 0.5, 1]$ are compared in Fig. 10(b) and (c).

As shown in the time interval $\bar{t} \in [2 \text{ s}, 5 \text{ s}]$, complete vibration suppression is again achieved once an exactly tuned DR is activated. However, when $\bar{t} \in [5 \text{ s}, 20 \text{ s}]$, the frequency mismatch, even if it is less than 1%, can significantly deteriorate the control performance, resulting in obvious residual vibrations. Moreover, the results that the deterioration is more apparent within $\bar{t} \in [10 \text{ s}, 15 \text{ s}]$ when the actual frequency is decreasing agree with Fig. 6(b). On the other hand, a nonlinear primary structure can beneficially exhibit smaller motion

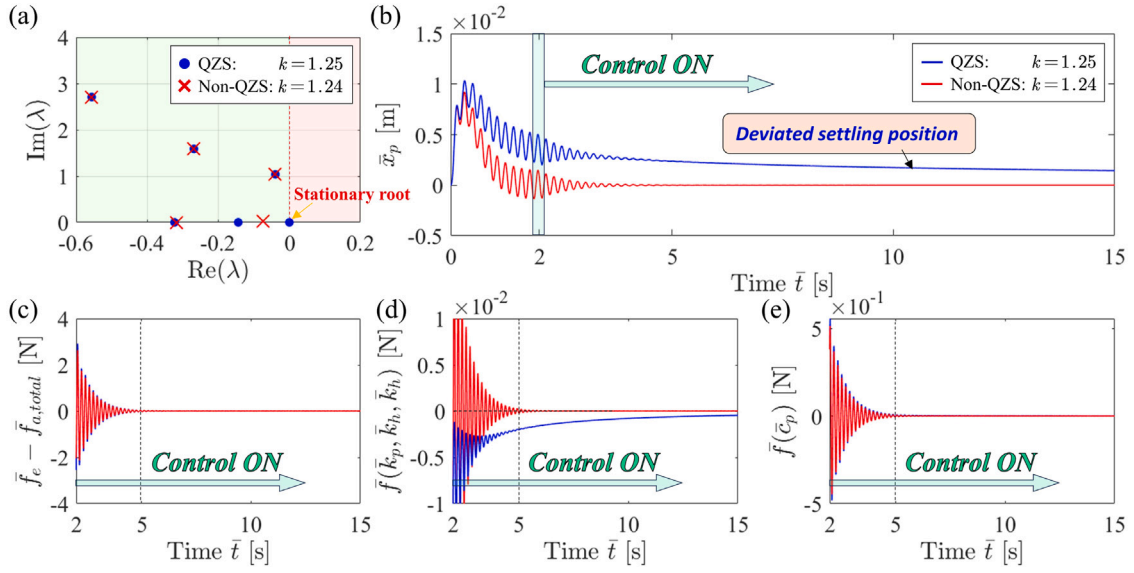


Fig. 9. Comparisons between the non-QZS ($k = 1.24$) and QZS ($k = 1.25$) cases. (a). Spectra of the characteristic Eq. (42). (b). Responses of the primary structure. (c). Time history of the force $\bar{f}_e - \bar{f}_{a,total}$. (d). Time history of the restoring force by the three springs $(\bar{k}_p, \bar{k}_h, \bar{k}_h)$. (e). Time history of the damping force by \bar{c}_p . The feedback actuation is activated at $\bar{t} = 2$ s.

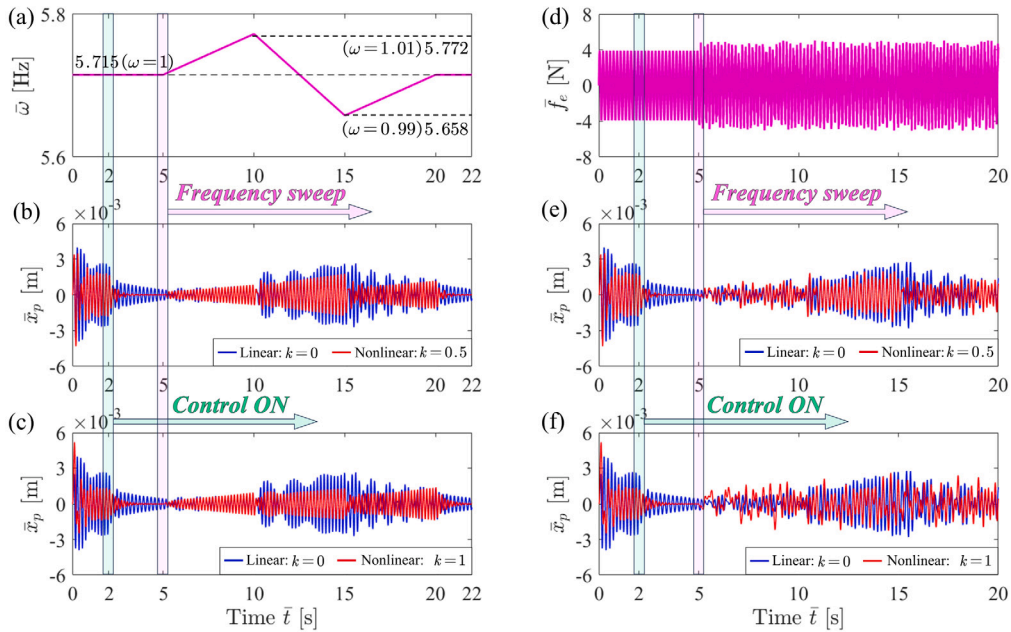


Fig. 10. Comparisons between the linear ($k = 0$) and nonlinear ($k = [0.5, 1]$) cases. (a). Time history of the excitation frequency. (b-c). Displacement responses of the primary structure. (d). Time history of the excitation force with noises. (e-f). Displacement responses of the primary structure under noisy excitations. The feedback actuation in (b,c,e,f) is activated at $\bar{t} = 2$ s.

amplitudes in both the passive case $\bar{t} < 2$ s and the active case $\bar{t} \in [5 \text{ s}, 20 \text{ s}]$ with frequency mismatches. Comparing Fig. 10(b) and (c), one can find that increasing the nonlinearity k can help suppress residual vibrations. However, the simultaneously raised response amplitude in the low-frequency band, as previously revealed in Fig. 6(a), deserves attention. The corresponding numerical tests are performed in Fig. 10(d-f), with noises additionally injected into the excitation when $\bar{t} \in [5 \text{ s}, 20 \text{ s}]$, leading to the time history of in Fig. 10(d). The low-pass effect mentioned in Section 6.1 can be observed by comparing Fig. 10(e) and (f). In addition, comparisons between Fig. 10(c) and (f) show that small noises can unfavorably neutralize the benefits of the nonlinearity in handling frequency mismatches. Further comparing

Fig. 10(e) and (f), the vibration suppression in the nonlinear case with a smaller (i.e.,) is still effective, and the nonlinearity improves control performance over the linear case. Thus, increasing to chase after benefits at extremities should be avoided, see also Remark 3.

7.4. Suppression of the residual vibrations due to frequency mismatches

Focusing on the time interval $\bar{t} \in [2 \text{ s}, 5 \text{ s}]$ of Fig. 10(b,c,e,f), one can find that the transient process for complete vibration suppression in the nonlinear case $k > 0$ is shorter than that in the linear case $k = 0$, which is the theoretical basis of Section 6.2. To test the effectiveness of Fig. 7, we still consider the excitation at the frequency $\omega = 1$. The

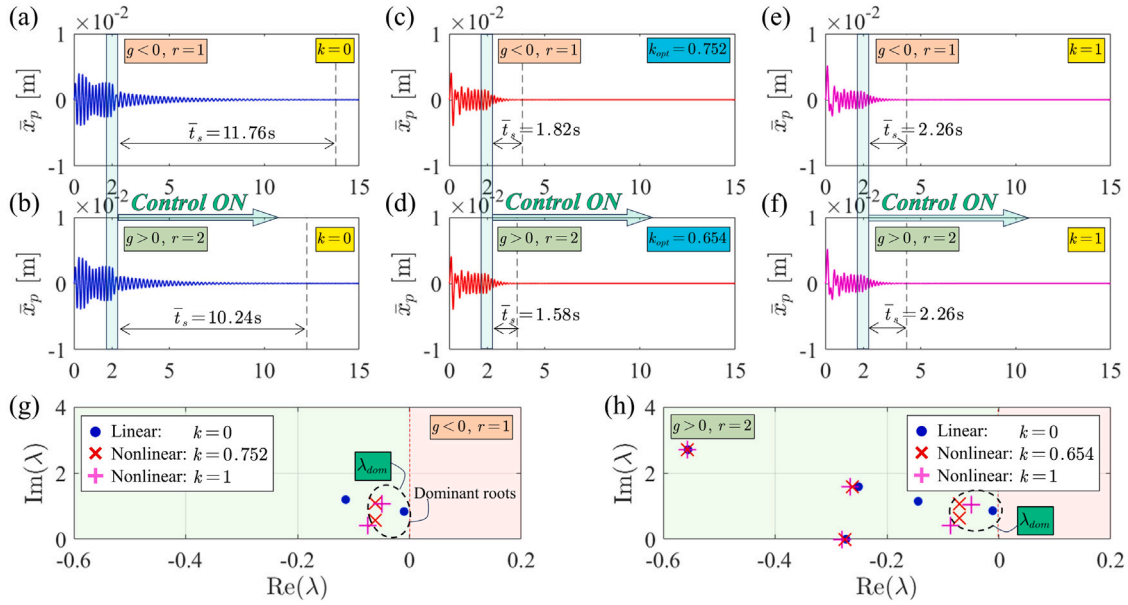


Fig. 11. Comparisons of transient process among different k values. (a-f). Numerical results when the DR is tuned with either ($g < 0, r = 1$) or ($g > 0, r = 2$). The feedback actuation is activated at $\bar{t} = 2$ s. (g-h). Spectra of the characteristic Eq. (42).

corresponding comparisons in both cases ($g < 0, r = 1$) and ($g > 0, r = 2$) are performed in Fig. 11.

The time histories of the responses \bar{x}_p of the primary structure concerning different k values are compared in Fig. 11(a-f), where the marked settling time \bar{t}_s is calculated by Eq. (50) and successfully predicts the duration of the transient process. This also indicates that system dynamics are within the basin of attraction of the stable equilibrium, i.e., Remark 1 is satisfied. Besides, the two optimal values $k_{opt} = [0.6545, 0.752]$ marked in Fig. 11(c) and (d), which correspond to the shortest \bar{t}_s , agree with Fig. 7(b). Spectra of the characteristic Eq. (42) in different cases are shown in Fig. 11(g) and (h), where the dominant root λ_{dom} first shifts leftward and then leftward as k increases, concurring with Fig. 7(a). Consequently, the nonlinearity $k > 0$ can enhance not only the steady-state performance for complete vibration suppression but also the transient process.

8. Conclusions

We aim to extend the DR concept from linear applications to completely suppress single-frequency vibrations on primary structures with nonlinear stiffness and to investigate the effect of such nonlinearity and how it can be used to enhance vibration control. Without loss of generality, a classic three-spring-two-link primary is considered to construct the nonlinear stiffness, with the delayed feedback actuation coupled between the absorber and the primary structure. The main results obtained for the delayed-coupled nonlinear dynamics, stability, and parametric effects are summarized as follows:

- Dynamical analysis is addressed using the harmonic balance method. However, no closed-form solutions exist due to the coupling between the delayed feedback actuation and system dynamics. To this end, an exclusive resultant-based procedure originating from our recent work [55] is generalized to facilitate calculation.
- Parameter tuning and equilibrium stability are both analytically tackled and numerically verified. The nonlinearity affects stability while posing no effect on parameter tuning. Besides, properly tuning such nonlinearity favorably extends the operable low-frequency band of the considered system (28) by up to 31%, see Fig. 5(b).

- The vibration suppression by a tuned DR can be complete since the nonlinear primary structure tends to be settled so that the vibrations at the fundamental frequency dominate dynamics, i.e., the first harmonic $i = 1$ in (15). However, it does not mean that the results in linear cases, where input and output frequencies are identical, can be directly used since the nonlinearity mainly alters the transient process rather than steady states, see Fig. 8.
- The nonlinearity of the primary structure can benefit vibration control by suppressing resonance peaks, extending the suppression region of anti-resonance (SROAR), achieving broadband vibration reduction, and expediting response speed. However, a QZS primary structure should be avoided to exclude the stationary root $\lambda = 0$, which leads to a deviated settling position, as shown in Fig. 9(b). In particular, the reduction of settling time by properly designing nonlinearity can be up to 84% as shown in Fig. 7 and Fig. 11. Hence, the nonlinearity of the primary structure can be treated as a novel mechanical or structural modification to enhance vibration absorption.
- Trade-off needs to be considered when increasing the nonlinearity to achieve extreme advantages in a specific aspect. Beneficially, keeping the nonlinearity within a reasonable value enhances the control performance in all aspects.

On the one hand, this work reveals the potential of the DR on nonlinear applications and provides the associated calculation tools and design and analysis rules to benefit further investigation. On the other hand, it shows how nonlinearity can benefit complete vibration absorption, a less-reported topic. With the established theories, our future work is interested in how to design a nonlinear DR for enhanced (complete) vibration suppression and how to address the associated nonlinear dynamics, a more complex task due to the more involved coupling between nonlinearity and delay.

CRediT authorship contribution statement

Yifan Liu: Conceptualization, Writing – review & editing, Writing – original draft. Li Cheng: Writing – review & editing, Supervision, Project administration.

Declaration of competing interest

The authors declare that they have no known competing financial interests or personal relationships that could have appeared to influence the work reported in this paper.

Data availability

The data that has been used is confidential.

Acknowledgments

This work is improved in the review process and in several communications with Prof. Nejat Olgac at the University of Connecticut.

Appendix

All Simulink models used in Section 7 can be found on the following website,

<https://drive.google.com/drive/folders/1IBpiHdsNzF5bNtpiyVR-9xSM11st7QFR?usp=sharing>.

References

- [1] N. Olgac, B. Holm-Hansen, A novel active vibration absorption technique: delayed resonator, *J. Sound Vib.* 176 (1994) 93–104.
- [2] H. Frahm, Device for damping vibrations of bodies, US patent 989 (1911).
- [3] J. Den Hartog, J. Ormondroyd, Theory of the dynamic vibration absorber, *ASME J. Appl. Mech.* 50 (1928) 11–22.
- [4] T. Vyhldal, N. Olgac, V. Kučera, Delayed resonator with acceleration feedback—complete stability analysis by spectral methods and vibration absorber design, *J. Sound Vib.* 333 (2014) 6781–6795.
- [5] M. Hosek, H. Elmali, N. Olgac, A tunable torsional vibration absorber: the centrifugal delayed resonator, *J. Sound Vib.* 205 (1997) 151–165.
- [6] N. Olgac, H. Elmali, S. Vijayan, Introduction to the dual frequency fixed delayed resonator, *J. Sound Vib.* 189 (1996) 355–367.
- [7] H. Elmali, M. Renzulli, N. Olgac, Experimental comparison of delayed resonator and PD controlled vibration absorbers using electromagnetic actuators, *J. Dyn. Syst. Meas. Control* 122 (2000) 514–520.
- [8] P.M. Nia, R. Sipahi, Controller design for delay-independent stability of linear time-invariant vibration systems with multiple delays, *J. Sound Vib.* 332 (2013) 3589–3604.
- [9] F.M. Alsalem, M.I. Younis, Stabilization of electrostatic MEMS resonators using a delayed feedback controller, *Smart Mater. Struct.* 19 (2010) 035016.
- [10] O. Eris, B. Aliok, A.F. Ergenc, A new delayed resonator design approach for extended operable frequency range, *J. Vib. Acoust.* 140 (2018) 041003.
- [11] D. Pilbauer, T. Vyhldal, N. Olgac, Delayed resonator with distributed delay in acceleration feedback—design and experimental verification, *IEEE/ASME Trans. Mechatronics* 21 (2016) 2120–2131.
- [12] V. Kučera, D. Pilbauer, T. Vyhldal, N. Olgac, Extended delayed resonators—design and experimental verification, *Mechatronics* 41 (2017) 29–44.
- [13] Y. Liu, N. Olgac, L. Cheng, Delayed resonator with multiple distributed delays—considering and optimizing the inherent loop delay, *J. Sound Vib.* (2024) 118290.
- [14] T. Vyhldal, D. Pilbauer, B. Aliok, W. Michiels, Analysis and design aspects of delayed resonator absorber with position, velocity or acceleration feedback, *J. Sound Vib.* 459 (2019) 114831.
- [15] D. Pilbauer, T. Vyhldal, W. Michiels, Optimized design of robust resonator with distributed time-delay, *J. Sound Vib.* 443 (2019) 576–590.
- [16] M. Kuře, J. Buřek, I. Boussaada, W. Michiels, S.-I. Niculescu, T. Vyhldal, Robust delayed resonator with acceleration feedback—design by double root assignment and experimental validation, *J. Sound Vib.* (2024) 118261.
- [17] J. Cai, Y. Liu, Q. Gao, Y. Chen, Spectrum-based stability analysis for fractional-order delayed resonator with order scheduling, *J. Sound Vib.* 546 (2023) 117440.
- [18] J. Cai, Q. Gao, Y. Liu, N. Olgac, Control design, analysis, and optimization of fractional-order delayed resonator for complete vibration absorption, *J. Sound Vib.* 571 (2024) 118083.
- [19] Y. Liu, J. Cai, N. Olgac, Q. Gao, A robust delayed resonator construction using amplifying mechanism, *J. Vib. Acoust.* 145 (1) (2023) 011010.
- [20] R. Jenkins, N. Olgac, Real-time tuning of delayed resonator-based absorbers for spectral and spatial variations, *J. Vib. Acoust.* 141 (2019) 021011.
- [21] N. Olgac, R. Jenkins, Actively tuned noncollocated vibration absorption: An unexplored venue in vibration science and a benchmark problem, *IEEE Trans. Control Syst. Technol.* 29 (2020) 294–304.
- [22] A. Saldanha, W. Michiels, M. Kuře, J. Buřek, T. Vyhldal, Stability optimization of time-delay systems with zero-location constraints applied to non-collocated vibration suppression, *Mech. Syst. Signal Process.* 208 (2024) 110886.
- [23] H. Silm, M. Kuře, J. Buřek, W. Michiels, T. Vyhldal, Spectral design and experimental validation of noncollocated vibration suppression by a delayed resonator and time-delay controller, *IEEE Trans. Control Syst. Technol.* (2023).
- [24] Z. Šika, T. Vyhldal, Z. Neusser, Two-dimensional delayed resonator for entire vibration absorption, *J. Sound Vib.* 500 (2021) 116010.
- [25] T. Vyhldal, W. Michiels, Z. Neusser, J. Buřek, Z. Šika, Analysis and optimized design of an actively controlled two-dimensional delayed resonator, *Mech. Syst. Signal Process.* 178 (2022) 109195.
- [26] Z. Šika, J. Krivořej, T. Vyhldal, Three dimensional delayed resonator of Stewart platform type for entire absorption of fully spatial vibration, *J. Sound Vib.* (2023) 118154.
- [27] M. Kani, S. Khadem, M. Pashaei, M. Dardel, Vibration control of a nonlinear beam with a nonlinear energy sink, *Nonlinear Dynam.* 83 (2016) 1–22.
- [28] D. Wagg, S. Neild, *Nonlinear Vibration with Control: For Flexible and Adaptive Structures*, Springer, 2010.
- [29] I. Kovacic, M.J. Brennan, *The Duffing Equation: Nonlinear Oscillators and their Behaviour*, John Wiley & Sons, 2011.
- [30] H. Ding, L.-Q. Chen, Nonlinear vibration of a slightly curved beam with quasi-zero-stiffness isolators, *Nonlinear Dynam.* 95 (2019) 2367–2382.
- [31] H. Ding, J. Ji, L.-Q. Chen, Nonlinear vibration isolation for fluid-conveying pipes using quasi-zero stiffness characteristics, *Mech. Syst. Signal Process.* 121 (2019) 675–688.
- [32] T. Deng, G. Wen, H. Ding, Z.-Q. Lu, L.-Q. Chen, A bio-inspired isolator based on characteristics of quasi-zero stiffness and bird multi-layer neck, *Mech. Syst. Signal Process.* 145 (2020) 106967.
- [33] Y. Wang, H.X. Li, C. Cheng, H. Ding, L.Q. Chen, Dynamic performance analysis of a mixed-connected inerter-based quasi-zero stiffness vibration isolator, *Struct. Control Health Monit.* 27 (2020) e2604.
- [34] X. Mao, M. Yin, H. Ding, X. Geng, Y. Shen, L. Chen, Modeling, analysis, and simulation of X-shape quasi-zero-stiffness-roller vibration isolators, *Appl. Math. Mech.* 43 (2022) 1027–1044.
- [35] G. Yan, Z.-Y. Wu, X.-S. Wei, S. Wang, H.-X. Zou, L.-C. Zhao, W.-H. Qi, W.-M. Zhang, Nonlinear compensation method for quasi-zero stiffness vibration isolation, *J. Sound Vib.* 523 (2022) 116743.
- [36] H. Ding, L.-Q. Chen, Shock isolation of an orthogonal six-DOFs platform with high-static-low-dynamic stiffness, *J. Appl. Mech.* 90 (2023) 111004.
- [37] L. Xiao, X. Sun, L. Cheng, X. Yu, A 3D-printed quasi-zero-stiffness isolator for low-frequency vibration isolation: modelling and experiments, *J. Sound Vib.* (2024) 118308.
- [38] J.-H. Yang, X.-D. Yang, Theoretical and experimental study of a novel nonlinear quasi-zero stiffness vibration isolator based on a symmetric link-rod-type structure, *Eng. Struct.* 301 (2024) 117284.
- [39] P. Ling, L. Miao, B. Ye, J. You, W. Zhang, B. Yan, Ultra-low frequency vibration isolation of a novel click-beetle-inspired structure with large quasi-zero stiffness region, *J. Sound Vib.* 558 (2023) 117756.
- [40] X. Sun, J. Xu, X. Jing, L. Cheng, Beneficial performance of a quasi-zero-stiffness vibration isolator with time-delayed active control, *Int. J. Mech. Sci.* 82 (2014) 32–40.
- [41] X. Sun, J. Xu, J. Fu, The effect and design of time delay in feedback control for a nonlinear isolation system, *Mech. Syst. Signal Process.* 87 (2017) 206–217.
- [42] X. Sun, S. Zhang, J. Xu, Parameter design of a multi-delayed isolator with asymmetrical nonlinearity, *Int. J. Mech. Sci.* 138 (2018) 398–408.
- [43] J. Xu, X. Sun, A multi-directional vibration isolator based on Quasi-Zero-Stiffness structure and time-delayed active control, *Int. J. Mech. Sci.* 100 (2015) 126–135.
- [44] X. Sun, F. Wang, J. Xu, Dynamics and realization of a feedback-controlled nonlinear isolator with variable time delay, *J. Vib. Acoust.* 141 (2019) 021005.
- [45] X. Sun, J. Xu, Vibration control of nonlinear absorber–isolator-combined structure with time-delayed coupling, *Int. J. Non-Linear Mech.* 83 (2016) 48–58.
- [46] C. Cheng, Y. Hu, R. Ma, W. Wang, Beneficial performance of a quasi-zero-stiffness vibration isolator with displacement-velocity feedback control, *Nonlinear Dynam.* 111 (2023) 5165–5177.
- [47] C. Cheng, S. Li, Y. Wang, X. Jiang, On the analysis of a high-static-low-dynamic stiffness vibration isolator with time-delayed cubic displacement feedback, *J. Sound Vib.* 378 (2016) 76–91.
- [48] B. Yan, X. Wang, H. Ma, W. Lu, Q. Li, Hybrid time-delayed feedforward and feedback control of lever-type quasi-zero-stiffness vibration isolators, *IEEE Trans. Ind. Electron.* 71 (2024) 2810–2819.
- [49] D. Huang, S. Zhou, R. Li, D. Yurchenko, On the analysis of the tristable vibration isolation system with delayed feedback control under parametric excitation, *Mech. Syst. Signal Process.* 164 (2022) 108207.
- [50] Y. Liu, B. Yan, L. Cheng, Dynamical analysis and design theory for active bistable vibration isolators considering delay effect, *J. Sound Vib.* 573 (2024) 118196.
- [51] J. Cai, Q. Gao, X. Zhang, Proportional-retarded control of a quasi-zero-stiffness vibration isolator, *J. Sound Vib.* (2024) 118309.
- [52] Y.-Y. Zhao, J. Xu, Effects of delayed feedback control on nonlinear vibration absorber system, *J. Sound Vib.* 308 (2007) 212–230.

- [53] X. Mao, W. Ding, Nonlinear dynamics and optimization of a vibration reduction system with time delay, *Commun. Nonlinear Sci. Numer. Simul.* 122 (2023) 107220.
- [54] F. Wang, X. Sun, H. Meng, J. Xu, Time-delayed feedback control design and its application for vibration absorption, *IEEE Trans. Ind. Electron.* 68 (2020) 8593–8602.
- [55] Y. Liu, J. Cai, L. Hou, B. Yan, L. Chen, Q. Gao, Bistable dynamics analysis using Padé approximation and resultant theory, *Int. J. Non-Linear Mech.* 149 (2023) 104325.
- [56] M. Krack, J. Gross, *Harmonic Balance for Nonlinear Vibration Problems*, Springer, 2019.
- [57] R.N. Jazar, *Perturbation Methods in Science and Engineering*, Springer, 2021.
- [58] X. Wang, H. Liu, Y. Chen, P. Gao, Beneficial stiffness design of a high-static-low-dynamic-stiffness vibration isolator based on static and dynamic analysis, *Int. J. Mech. Sci.* 142 (2018) 235–244.
- [59] W. Wu, X. Chen, Y. Shan, Analysis and experiment of a vibration isolator using a novel magnetic spring with negative stiffness, *J. Sound Vib.* 333 (2014) 2958–2970.
- [60] J.J. Sylvester, XxIII. A method of determining by mere inspection the derivatives from two equations of any degree, *Lond., Edinb., Dublin Philos. Mag. J. Sci.* 16 (1840) 132–135.
- [61] G.E. Collins, The calculation of multivariate polynomial resultants, *J. ACM* 18 (1971) 515–532.
- [62] A. Edelman, H. Murakami, Polynomial roots from companion matrix eigenvalues, *Math. Comp.* 64 (1995) 763–776.
- [63] S.C. Stanton, B.A. Owens, B.P. Mann, Harmonic balance analysis of the bistable piezoelectric inertial generator, *J. Sound Vib.* 331 (2012) 3617–3627.
- [64] V.B. Kolmanovskii, V.R. Nosov, *Stability of Functional Differential Equations*, Elsevier, 1986.
- [65] N. Olgac, R. Sipahi, An exact method for the stability analysis of time-delayed linear time-invariant (LTI) systems, *IEEE Trans. Automat. Control* 47 (2002) 793–797.
- [66] Y. Liu, J. Cai, H. Li, Q. Gao, Optimal design and sensitivity analysis of the dynamic vibration absorber with amplifying mechanism, *J. Comput. Inf. Sci. Eng.* 23 (2023) 051005.
- [67] T. Vyhldal, P. Zítek, Mapping based algorithm for large-scale computation of quasi-polynomial zeros, *IEEE Trans. Automat. Control* 54 (2009) 171–177.
- [68] N. Olgac, R. Sipahi, A.F. Ergenc, 'Delay scheduling', an unconventional use of time delay for trajectory tracking, *Mechatronics* 17 (2007) 199–206.
- [69] R. Cepeda-Gomez, N. Olgac, A consensus protocol under directed communications with two time delays and delay scheduling, *Internat. J. Control* 87 (2014) 291–300.